ACS NANO

Cite This: ACS Nano 2018, 12, 5504−5517

www.acsnano.org

ARTICLE

Exploration of Near-Infrared-Emissive Colloidal Multinary Lead Halide Perovskite Nanocrystals Using an Automated Microfluidic Platform

Ioannis Lignos,[†,¶] Viktoriia Morad,[†,‡,§] Yevhen Shynkarenko,[‡,§] Caterina Bernasconi,[‡,§] Richard M. Maceiczyk,[†] Loredana Protesescu,[‡,§] Federica Bertolotti,[∥,⊥] Sudhir Kumar,[†] Stefan T. Ochsenbein,[‡,§] Norberto Masciocchi,[∥] Antonietta Guagliardi,[#] Chih-Jen Shih,[†] Maryna I. Bodnarchuk,[*,§] Andrew J. deMello,[*,†] and Maksym V. Kovalenko[*,‡,§]

[†]Institute for Chemical and Bioengineering, Department of Chemistry and Applied Biosciences, ETH Zürich, Vladimir-Prelog-Weg 1, Zürich 8093, Switzerland

[‡]Institute of Inorganic Chemistry, Department of Chemistry and Applied Biosciences, ETH Zürich, Vladimir-Prelog-Weg 1, Zürich 8093, Switzerland

[§]Empa-Swiss Federal Laboratories for Materials Science and Technology, Überlandstrasse 129, Dübendorf 8600, Switzerland

[∥]Dipartimento di Scienza e Alta Tecnologia and To.Sca.Lab, Università dell'Insubria, Via Valleggio 11, I-22100 Como, Italy

[⊥]Aarhus Institute of Advanced Studies (AIAS), Aarhus University, Høegh-Guldbergs Gade 6B, 8000 Aarhus C, Denmark

[#]Istituto di Cristallografia, Consiglio Nazionale delle Ricerche, and To.Sca.Lab, via Valleggio 11, I-22100 Como, Italy

Supporting Information

ABSTRACT: Hybrid organic−inorganic and fully inorganic lead halide perovskite nanocrystals (NCs) have recently emerged as versatile solution-processable light-emitting and light-harvesting optoelectronic materials. A particularly difficult challenge lies in warranting the practical utility of such semiconductor NCs in the red and infrared spectral regions. In this context, all three archetypal A-site monocationic perovskites—$CH_3NH_3PbI_3$, $CH(NH_2)_2PbI_3$, and $CsPbI_3$—suffer from either chemical or thermodynamic instabilities in their bulk form. A promising approach toward the mitigation of these challenges lies in the formation of multinary compositions (mixed cation and mixed anion). In the case of multinary colloidal NCs, such as quinary $Cs_xFA_{1-x}Pb(Br_{1-y}I_y)_3$ NCs, the outcome of the synthesis is defined by a complex interplay between the bulk thermodynamics of the solid solutions, crystal surface energies, energetics, dynamics of capping ligands, and the multiple effects of the reagents in solution. Accordingly, the rational synthesis of such NCs is a formidable challenge. Herein, we show that droplet-based microfluidics can successfully tackle this problem and synthesize $Cs_xFA_{1-x}PbI_3$ and $Cs_xFA_{1-x}Pb(Br_{1-y}I_y)_3$ NCs in both a time- and cost-efficient manner. Rapid *in situ* photoluminescence and absorption measurements allow for thorough parametric screening, thereby permitting precise optical engineering of these NCs. In this showcase study, we fine-tune the photoluminescence maxima of such multinary NCs between 700 and 800 nm, minimize their emission line widths (to below 40 nm), and maximize their photoluminescence quantum efficiencies (up to 89%) and phase/chemical stabilities. Detailed structural analysis revealed that the $Cs_xFA_{1-x}Pb(Br_{1-y}I_y)_3$ NCs adopt a cubic perovskite structure of $FAPbI_3$, with iodide anions partially substituted by bromide ions. Most importantly, we demonstrate the excellent transference of reaction parameters from microfluidics to a conventional flask-based environment, thereby enabling up-scaling and further implementation in optoelectronic devices. As an example, $Cs_xFA_{1-x}Pb(Br_{1-y}I_y)_3$ NCs with an emission maximum at 735 nm were integrated into light-emitting diodes, exhibiting a high external quantum efficiency of 5.9% and a very narrow electroluminescence spectral bandwidth of 27 nm.

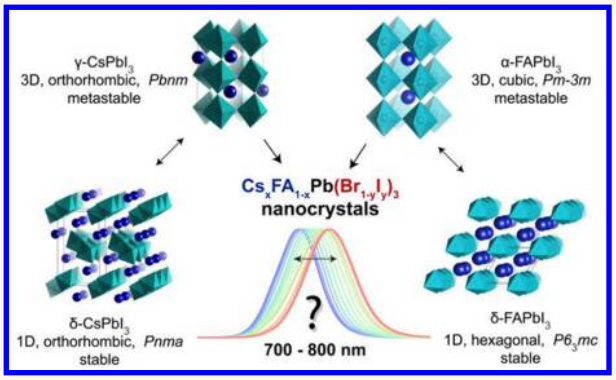

KEYWORDS: *perovskites, microfluidics, nanocrystals, formamidinium, quantum dots, halides*

Lead halide perovskites (LHP) of the $APbX_3$ type, where A can be methylammonium (MA, $CH_3NH_3^+$), formamidinium (FA, $CH_3(NH_2)_2^+$), inorganic cations (Cs^+, Rb^+), or a

Received: February 9, 2018
Accepted: May 12, 2018
Published: May 12, 2018

DOI: 10.1021/acsnano.8b01122
ACS Nano 2018, 12, 5504−5517

mixture thereof and X is a halide (Br, I, and their mixtures), have attracted enormous attention after they were recognized as efficient thin-film absorber materials for photovoltaics, with power conversion efficiencies of up to 22.7%.[1−4] Recently, there has been a surge of studies on the nanoscale counterparts of these perovskites and, in particular, on colloidal nanocrystals (NCs),[5−12] which hold great promise as versatile photonic sources for displays, lighting, light-emitting diodes (LEDs), and lasers[13−16] and as light harvesters for solar cells and photodetectors.[1,17] Unlike other forms of $APbX_3$ perovskites—bulk single and polycrystals, thin films, and other substrate-grown structures—colloidal NCs have a particular set of advantages, foremost of which is their versatile solution processability and miscibility with other materials, as well as access to quantum-size effects and their facile surface- and shape-engineering.[18] To date, essentially all work on colloidal $APbX_3$ NCs has concentrated on those compositions, which emit in the visible region of the electromagnetic spectrum (between 400 and 700 nm), with $CsPbBr_3$ and $FAPbBr_3$ NCs, exhibiting green photoluminescence (PL, between 500 and 550 nm), being by far the most popular targets. This can be attributed to the high durability of these bromides, as compared to other compositions in the $APbX_3$ family.

In the current study, we focus our attention on multinary perovskite NCs of the quinary composition $Cs_xFA_{1-x}Pb(Br_{1-y}I_y)_3$, with a view to controlling their optical properties in the near-infrared (700−800 nm). It should be noted that there is extensive literature regarding red and near-infrared emissive colloidal $MAPbI_3$ NCs, refs 7 and 19−23 being representative examples. However, $MAPbI_3$ NCs suffer from severe instabilities caused by humidity, light, and heat and eventually decompose into CH_3NH_2, PbI_2, HI, and I_2.[22,24,25] Fully inorganic $CsPbX_3$ NCs (X = Cl, Br, and I), synthesized by a hot injection method, exhibit tunable emission between 410 and 700 nm and high PL quantum efficiencies (50−90%).[6] Presently, $CsPbX_3$ NCs are the focus of attention with respect to their chemical engineering (*i.e.*, identification of precursors, growth kinetics, shape-control, postsynthetic reactivity, and up-scaling),[20,26−45] surface chemistry,[8,46−50] photophysics (single-dot spectroscopy, lasing, *etc.*),[51−59] and applications in television displays,[6,60−62] light-emitting devices,[50,63−68] and solar cells.[17] The usability of red-emissive $CsPbX_3$ NCs is, however, strongly limited by the phase instability of the 3D polymorphs of $CsPbI_3$. For similar reasons, iodide-rich $CsPb(Br/I)_3$ compositions are also unstable. As for FA-based analogues, which benefit from the higher chemical stability of the FA ion (compared to that of MA^+), one-pot colloidal syntheses have led to the development of stable and highly emissive FA-doped $CsPbI_3$ NCs (PL peak at *ca.* 690 nm; *ca.* 10% FA) and $FAPbI_3$ NCs (PL peak at *ca.* 780 nm),[69] with cubic or nearly cubic NC shapes and mean particle sizes between 10 and 20 nm. Interestingly, unlike colloidal $FAPbI_3$ NCs, bulk $FAPbI_3$ is completely unstable due to a phase transition from semiconductive perovskite into a yellow, nonperovskite phase (an observation that will be further discussed in the Results and Discussion section of this study). A formidable challenge with iodide-based NCs lies in discovering the compositional space and related synthesis parameters that would provide for continuous coverage of the 700−800 nm spectral range with narrow PL line widths and without compromising the chemical durability of the NCs.

Our choice of the quinary composition, $Cs_xFA_{1-x}Pb(Br_{1-y}I_y)_3$, was motivated by previous thin-film and bulk single-crystal studies,[70−74] which indicate that the concomitant incorporation of Cs and Br into the $FAPbI_3$ lattice stabilizes the 3D perovskite phase and allows for the compositional tuning of band-gap energy through the formation of mixed-halide solid solutions.[75] With monohalide $FAPbI_3$ and $FA_{0.1}Cs_{0.9}PbI_3$ NCs, the only way to access the entire 700−800 nm range is to exploit quantum-size effects and reduce NC size to the 3−8 nm range. Such small NCs are highly labile morphologically, and their PL characteristics are consequently broad and unstable.[76]

In the case of NCs, accessing suitable reaction parameters for the formation of stable $Cs_xFA_{1-x}PbX_3$ NCs with tunable emission maxima in the range of 700−780 nm is simply not possible with flask reactions.[69] Specifically, in a recent study on the formation of mixed-anion $FAPbX_3$ NCs, it was reported that variation in the Br−I content led solely to two stable compositions, one emitting at 680 nm and the other at 760 nm.[69] This is due to the fact that in NCs the ability to form certain compositions is governed not only by the thermodynamics of the mixed-ion phases but also by the NC surfaces (*i.e.*, surface energy and ligand binding) and chemical equilibria with the precursors in the solution. These factors greatly expand relevant parametric space beyond the mixing ratios of the Cs, FA, Pb, and halide precursors, thus making thorough exploratory synthesis and optimization virtually impossible with conventional flask-based techniques.

Recently, we showcased the potential of droplet-based microfluidics combined with online absorption and PL spectroscopy in discovering the optimal synthesis parameters for ternary and quaternary (mixed-anion) $CsPbX_3$ NCs[77] and $FAPbX_3$[78,79] NCs. The next logical step, which is pursued in this work, is the exploration of NCs of higher compositional complexity, *i.e.*, $Cs_xFA_{1-x}Pb(Br_{1-y}I_y)_3$ NCs. In such cases, the use of high-throughput automated microfluidic reactors becomes an absolute necessity for rapid and detailed experimentation. Using microfluidics, we herein demonstrate the formation of $Cs_xFA_{1-x}Pb(Br_{1-y}I_y)_3$ NCs with PL peak tuning between 690 and 780 nm and narrow PL line widths (expressed as full width at half-maximum, fwhm). Characterization by X-ray diffraction (XRD) and elemental analysis pointed to the incorporated quantities of Cs (0.1−1.2% with respect to FA) and Br (10−18% with respect to I). The obtained $Cs_xFA_{1-x}Pb(Br_{1-y}I_y)_3$ NCs were approximately cubic in shape, with a mean size of 8−13 nm. The reaction parameters were fully transferrable from our microfluidic platform (pL−nL scale) to conventional reaction flasks (mL scale). This allows us to demonstrate the optoelectronic utility of these NCs by fabricating near-infrared LEDs with an external quantum efficiency (EQE) up to 5.9% at 735 nm.

RESULTS AND DISCUSSION

Formability of $APbI_3$. To obtain red to near-infrared emissive $Cs_xFA_{1-x}Pb(Br_{1-y}I_y)_3$ compositions, the structural chemistry of these perovskites must be considered: only those polymorphs of $APbI_3$ compounds that retain three-dimensional (3D) corner-shared interconnections of lead halide octahedra are potent semiconductors. The extended electronic structure in lead halide perovskites arises from the periodic 3D network of PbX_6 octahedra. Low-dimensionality polymorphs of the same composition exhibit higher (by at least 1 eV) and often indirect band gaps, typically on the order of 300−500 nm. 3D polymorphs of all archetypal ternary $APbI_3$ compounds have stability issues. $MAPbI_3$ is chemically unstable, whereas the 3D polymorphs of $CsPbI_3$ and $FAPbI_3$ are thermodynamically metastable and undergo transitions into 1D polymorphs (Figure 1).[76,80−85] Interestingly, the thin-film and nanoscale forms of $CsPbI_3$ and $FAPbI_3$ exhibit extended but still finite stability in their 3D

DOI: 10.1021/acsnano.8b01122
ACS Nano 2018, 12, 5504−5517

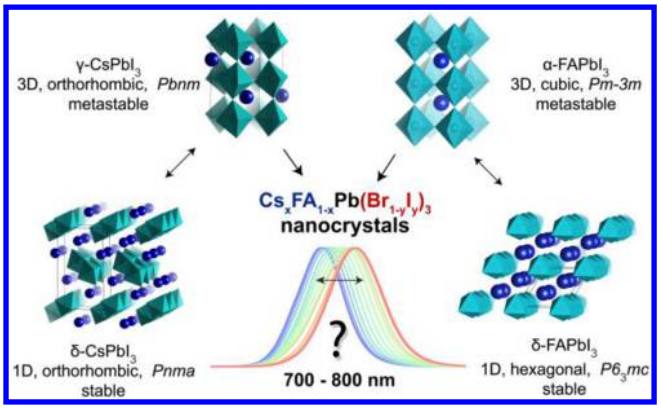

Figure 1. Formabilities of the 3D and 1D polymorphs of $CsPbI_3$ and $FAPbI_3$ compounds and the goal of this study: near-infrared emissive LHP NCs. The PbI_6 octahedra of α-$FAPbI_3$ NCs are assembled in a 3D cubic metastable lattice, which spontaneously converts into a 1D hexagonal version (nonluminescent) at room temperature. In the case of $CsPbI_3$, the PbI_6 octahedra of $FAPbX_3$ NCs are assembled in a 3D orthorhombic metastable lattice (γ-phase), which eventually converts at room temperature into a 1D orthorhombic δ-phase (nonluminescent). The goal of this study is highlighted with a question: can high-throughput microfluidic screening identify the existence of stable multinary $Cs_xFA_{1-x}Pb(Br_{1-y}I_y)_3$ phases in the form of colloidal NCs, which cover the PL region of 700−800 nm, *i.e.*, in-between ternary 3D phases ($CsPbI_3$ and $FAPbI_3$)? We note that bulk α-$FAPbI_3$ emits at 840 nm and γ-$CsPbI_3$ emits at 710 nm, whereas their NC counterparts are commonly reported to emit at ≤700 and ≤780 nm, respectively.[6,8−12,69] It is also noted that the space groups reported for the γ- and δ-phases of $CsPbI_3$ do not differ (while their structures manifestly do), as they can easily be interconverted by simple axis permutations. We used the original *Pbnm* and *Pnma* for the γ- and δ-forms, respectively, to maintain consistency with past literature.

polymorph forms (from days to several months), primarily due to surface effects.[6,32,69,86−88]

Thermodynamic instability is caused by the Cs and FA ions being, respectively, slightly too small and too large for the voids in between PbI_6 octahedra. This has been broadly discussed in the literature in terms of the Goldsmith tolerance factor (t) and octahedral factor (μ), which describe the optimal dense packing of charged ions in an ideal cubic 3D perovskite.[72,89−93] Mixing larger and smaller ions at the A-site is a powerful strategy for adjusting the geometric fitness of the A-cation in the void space of the 3D lead halide framework, thereby improving its phase stability. A high entropy of mixing is also considered to be a stabilizing factor.[71] In fact, the best phase stabilities and optoelectronic performances have been reported for thin films with such mixed A-site occupations: FA/MA,[94−97] Cs/MA,[98] Cs/FA,[70−73] Cs/MA/FA,[99] or even Rb/Cs/MA/FA.[4]

Toward Multinary $APbX_3$ Perovskites: The Goal of This Investigation. Covering the desired spectral range of 700−800 nm requires broad mapping in Cs-FA perovskites, because 3D $CsPbI_3$ and $FAPbI_3$ exhibit band gaps of 1.75 eV (710 nm) and 1.48 eV (840 nm), respectively. From the viewpoint of structural chemistry, it remains unclear which crystal structures will be adopted or are stable when Cs:FA and Br:I ratios are adjusted simultaneously, as the parent Cs and FA compounds have different 3D polymorph structures (Figure 1). We recently found that for bulk single crystals, in accordance with previous studies on thin films starting with α-$FAPbI_3$, one can concomitantly introduce up to 15% Cs and 30% Br, while maintaining the same cubic crystal structure as α-$FAPbI_3$.[74]

As for colloidal NCs, we recently reported the synthesis of a mixed-cationic composition, $Cs_{0.9}FA_{0.1}PbI_3$, with the same crystal structure as orthorhombic 3D γ-$CsPbI_3$, *via* a flask-based process.[69] Multiple variations of the Cs:FA reagent ratio and synthesis temperatures led to the same composition (with *ca.* 10% FA). From these studies, it can be surmised that the exploration of complex compositions is prohibitively difficult *via* flask-based syntheses. This is because with one iteration of only one parameter per synthesis (each lasting several hours when conducted manually) several years will be required to properly map compositional space and other factors, such as the effects of ligands, solvents, and solvation equilibria.

Experimental Design and Combinatorial Strategy. Microfluidic reactors allow for the addition of multiple reagents in a user-defined manner, rapid thermal and mass transfer, and quantitative kinetic investigation of reactions, thus defining an ideal medium for preparing semiconductor NCs with well-defined morphologies and physicochemical properties.[100−103] In addition, the advances in robust microfluidic configurations,[100,103] real-time detection methods,[104−111] continuous purification[112,113] and ligand-exchange[114] systems, and optimization algorithms[115−117] make microfluidic reactors ideal for the detailed investigation of rapid and complex reaction kinetics[77,78,106,118] and for the discovery of multicomponent semiconductor NCs.[77,78,119]

Herein, we modified and applied a previously developed microfluidic platform that had been used for the synthesis and real-time characterization of binary chalcogenide NCs[106] and $CsPbX_3$ NCs.[77] This platform (see Figure 2 and associated description in the Methods section) incorporates a multiphase microfluidic reactor with integrated PL and absorption detection to rapidly screen reaction conditions. The controlled injection of precursor solutions (Cs-oleate, FA-oleate, PbX_2, and PbY_2) and carrier fluid is performed in an automated manner (using syringe pumps), allowing for the formation of nanoliter droplets using a seven-port manifold and efficient mixing of precursors (in ∼300 ms).[77] In the case of $Cs_xFA_{1-x}PbX_3$ (X = Br and I) NCs, we defined four interdependent molar ratios, which were adjusted during synthesis: FA/Pb, Cs/Pb, Br/I, and Cs/FA. In this report, the latter is presented as the Cs percentage relative to the FA content. A tube-based microfluidic reactor allows for rapid heating of the droplets (within a few hundred ms), along with the real-time extraction of PL and absorption characteristics at various reaction times (0.1−20 s) and temperatures (25−130 °C). Additional characterization of the synthesized NCs by transmission electron microscopy (TEM) and XRD was conducted in an off-line manner, by collecting a sufficient quantity of the sample during synthesis at a fixed set of reaction conditions (see the Methods section for details). The optimized parameters were then transferred to conventional flask-based reactions.

Synthesis of $Cs_xFA_{1-x}PbI_3$ NCs. In our previous study, we showed that $FAPbI_3$ NCs can grow even at room temperature,[78] while $CsPbI_3$ NCs with a 3D phase are formed at temperatures above 100 °C.[77] Accordingly, we decided that analyzing the temperature range suitable for the formation of $Cs_xFA_{1-x}PbI_3$ NCs was an important initial task. Figure 3a−c report the variation in emission line width and PL peak at 25−130 °C (FA/Pb = 9.3, Cs/Pb = 0.3, and %Cs = 3.0). The formation of $FAPbI_3$ NCs takes place at room temperature, which can be inferred by the emergence of the PL peak at 792 nm, consistent with a previous flask-based synthetic study, in which 15 nm $FAPbI_3$ NCs exhibited a PL peak at 780 nm.[69] Higher temperatures led to a rapid increase in the band-gap energy, which we ascribe to the

DOI: 10.1021/acsnano.8b01122
ACS Nano 2018, 12, 5504−5517

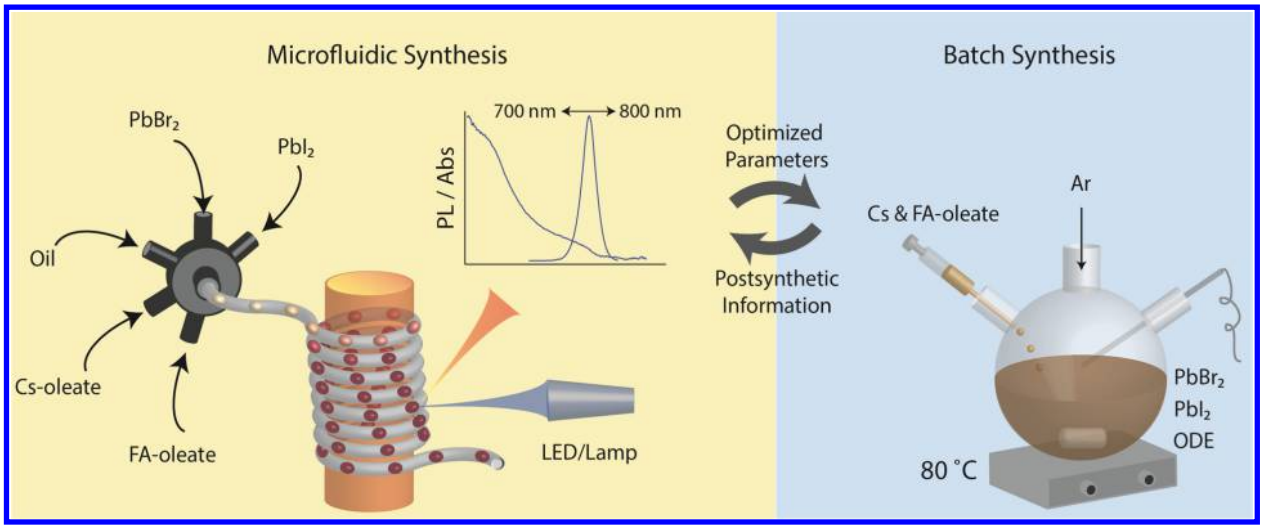

Figure 2. (Left) Illustration of the segmented-flow reaction platform equipped with online PL and absorbance modules for the synthesis and real-time monitoring of $Cs_xFA_{1-x}PbX_3$ perovskite NCs. The microfluidic platform allows for a systematic and independent variation of precursor molar ratios, such as Cs/Pb, FA/Pb, Cs/FA, and Br/I, growth times (determined by the flow rate and tube lengths), and temperature. Droplets are generated by adjusting the flow rates of the carrier phase (50−200 μL/min) and that of the dispersed phase (1.2−50 μL/min). (Right) Illustration of a typical flask-based hot-injection synthesis of $Cs_xFA_{1-x}PbX_3$ NCs. Overall, synthesis optimization was performed by mutual information exchange between flask-based experimentation (identification of suitable precursors, solvents, and capping ligands) and microfluidics (optimization of the reaction parameters). The optimized reaction parameters were successfully transferred from microfluidics back into flask reactors, followed by up-scaling and additional postsynthetic characterization (XRD, electron microscopy, and stability tests).

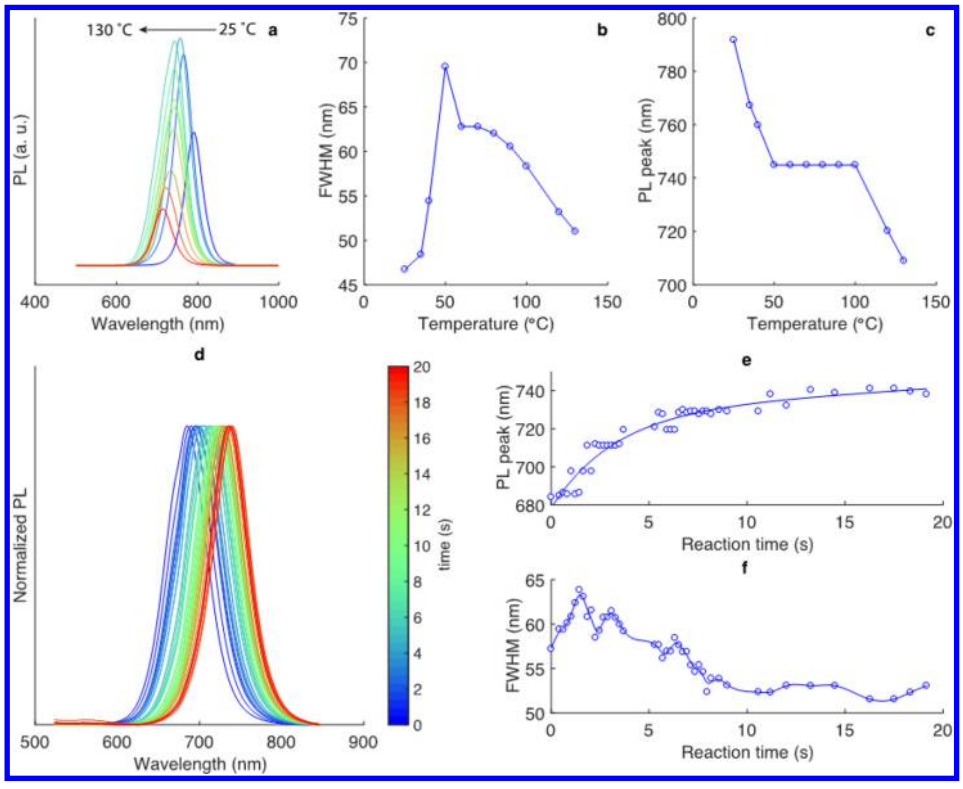

Figure 3. Microfluidic synthesis of $Cs_xFA_{1-x}PbI_3$ NCs. Variation in the (a) PL spectra, (b) fwhm, and (c) PL maximum as a function of temperature for $Cs_{0.03}FA_{0.97}PbI_3$ NCs (with the variation in the Cs/FA molar ratio indicated). Other parameters were as follows: FA/Pb = 9.3, Cs/Pb = 0.3, and reaction time = 10 s. (d−f) Temporal evolution of the normalized online PL spectra, PL maxima, and fwhm of $Cs_{0.02}FA_{0.98}PbI_3$ NCs at 80 °C.

incorporation of Cs. The possibility of smaller NC sizes (quantum dots 3−10 nm in diameter) causing larger band gaps can be discounted using postsynthesis TEM images, with all NCs obtained in this study for growth times greater than 7 s being 15−20 nm in size. Size evolution occurs very quickly and over the course of several seconds. From 50 to 90 °C, the PL peak remained stable at 740−745 nm (Figure 3c), but with a gradually decreasing fwhm. Higher synthesis temperatures (>110 °C) resulted in PL peaks closer to 700 nm, most likely due to the formation of ternary $CsPbI_3$ NCs with or without minimal

DOI: 10.1021/acsnano.8b01122
ACS Nano 2018, 12, 5504−5517

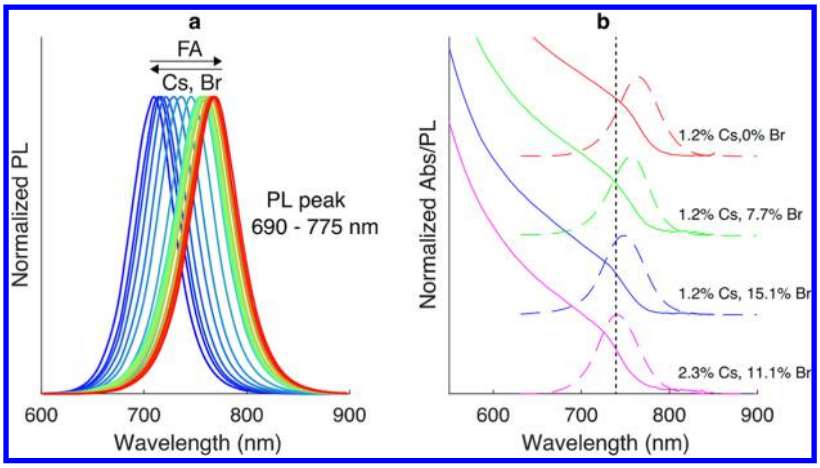

Figure 4. (a) PL spectra of colloidal $Cs_xFA_{1-x}Pb(Br_{1-y}I_y)_3$ NCs synthesized using the microfluidic platform and exhibiting composition-tunable band-gap energies between 690 and 780 nm with fwhm values of 40−65 nm and (b) representative online PL and in online absorption spectra at different quantities of Cs^+ and Br^- in the reaction mixture.

incorporation of FA ions. Accordingly, we concluded that the 50−90 °C range is ideal for compositional engineering purposes.

The high speed of formation of $Cs_{0.02}FA_{0.98}PbI_3$ NCs is on par with $FAPbX_3$ (see ref 78 and Figure S1) and $CsPbI_3$ (reported previously),[77] taking only a few seconds to stabilize the PL maximum at 740 nm and the fwhm at 52 nm (Figure 3d−f). Off-line optical characterization after synthesis indicates that there is no subsequent growth or other form of evolution in the $Cs_xFA_{1-x}PbI_3$ NCs (see Figure S2). Based on these observations, further rapid automated screening, at a rate of 100 adjustments per synthesis parameter per hour, was carried out with reaction times of at least (and typically) 7 s.

The efficiency of Cs incorporation is expected to depend not only on temperature but also on the solvation conditions and Cs/FA ratio and to some extent on the Cs/Pb and FA/Pb ratios. Because these relationships are not fully and rationally predictable when the equilibrium constants and involved energies (lattice energies for all compositions, solvation energies, surface energies, and ligand binding energies) are not completely known, they were tested in this study in a combinatorial fashion (Figures S3−S6). In brief, for excess FA (by a factor of 6 with respect to Pb), a narrow fwhm can be obtained (Figure S3). At much higher FA/Pb ratios (>13), the crystal phase of the NCs tends to change from black to yellow within hours of synthesis. The TEM images revealed severe morphological irregularities in such NCs, which were in the form of large populations of micrometer-sized needles and rods (Figure S4). Furthermore, the PL tunability of $Cs_xFA_{1-x}PbI_3$ NCs was limited to Cs/Pb ratios lower than 2 and Cs loadings of ≤10% (Figure S3). Outside this window, the PL maxima were always in the range of 680−700 nm, suggesting the formation of pure $CsPbI_3$ NCs or their mixtures with other compositions (seen as multi-Gaussian PL lines; see Figure S3e, for Cs content equal to 23.3%) or perhaps even mixtures of various shapes. The TEM images (Figure S4, S5) illustrate how the three interlinked ratios affect the morphology of the synthesized $Cs_xFA_{1-x}PbI_3$ NCs. Progressive addition of 0.3−5.2% Cs^+ (with respect to the FA content) continuously tunes the PL maximum from 758 to 710 nm (Figure S6), while maintaining a narrow fwhm in the range of 48−55 nm. Although the XRD results suggest that mixed perovskites adopt a structure similar to that of pure $FAPbI_3$ (Figure S7), the majority of $Cs_xFA_{1-x}PbI_3$ NC samples exhibited low colloidal and chemical stabilities, except those samples with both low FA/Pb ratios (≤7) and low Cs loadings (up to 2%).

Synthesis of $Cs_xFA_{1-x}Pb(Br_{1-y}I_y)_3$ NCs. The addition of Br into the system was then explored as a way of stabilizing crystal structure and tuning the PL maximum in the desired range (700−800 nm). The operating temperature and reaction times were similar to those used for the synthesis of $Cs_xFA_{1-x}PbI_3$ NCs. As the addition of a second halide further increases the complexity of the synthetic system and can shift the product equilibrium toward other perovskite compositions, parametric screening must be performed with caution. We therefore broadly explored the influence of the interdependent molar ratios of Cs/Pb, FA/Pb, and Br^- content on the optical properties and stability of the Br/I mixtures (as illustrated in Figures S8−S10). In brief, such a combinatorial study revealed that the parametric zones of the FA/Pb and Cs/Pb molar ratios, able to tune the PL peak between 690 and 780 nm (while maintaining a satisfactory fwhm), were 2.5−6.0 and 0.01−0.04, respectively (Figure S9). In addition, Br loading of up to 15% leads to a linear blue shift of the emission band at all FA/Pb molar ratios (Figure S10). A key message here is that in nearly all optimized compositions Br addition does not alter the emission line width or emission intensity, suggesting that the synthesized NCs have stable optical characteristics. Furthermore, an increase in Br^- loading over 25% will deliver perovskite NCs with emission energies in the range of 650−720 nm. However, such an increase in Br^- loading can trigger the formation of other perovskite structures, such as $FAPb(Br_{1-y}I_y)_3$ NCs, due to excess FA-oleate in the reaction system (Figure S11).

Figure 4a presents selected PL spectra in the range of 690 to 775 nm, with fwhm in the range of 45−65 nm. Such precise PL tuning is achieved through a systematic variation of all three interlinked molar ratios within their refined parametric zones. In particular, variation in Cs (in the range of 0.2−5.2%) and Br (between 0% and 15% of the total halide concentration) content leads to a blue shift in the in-line (*i.e.*, postheating and when the reaction was quenched) absorption and PL spectra (Figure 4b). Most importantly, the incorporation of up to 15% Br^- into the structure of $Cs_xFA_{1-x}PbI_3$ NCs increased the period of stability of the $Cs_xFA_{1-x}PbI_3$ NCs from several hours to several weeks (Figure S12).

Transfer to Flask-Based Synthesis. To assess whether the optimal parameters can be transferred to conventional

DOI: 10.1021/acsnano.8b01122
ACS Nano 2018, 12, 5504−5517

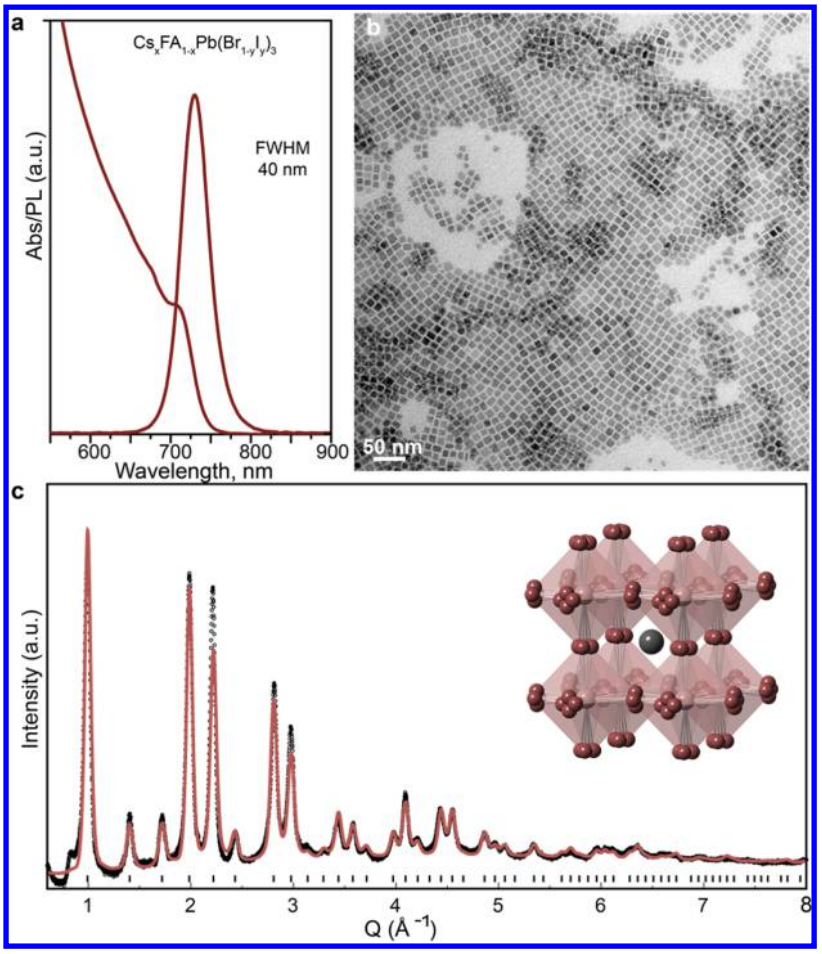

Figure 5. Optical absorption and PL spectra of $Cs_xFA_{1-x}Pb(Br_{1-y}I_y)_3$ NCs synthesized in conventional flask reactors, exhibiting a fwhm of 40 nm. (b) Bright-field scanning TEM (STEM) image of $Cs_xFA_{1-x}Pb(Br_{1-y}I_y)_3$ NCs. (c) Synchrotron XRD pattern (black) and best fit (red, 2θ range of 0.5−130°; λ = 0.563 729 Å) for $Cs_xFA_{1-x}Pb(Br_{1-y}I_y)_3$ NCs, yielding a refined lattice parameter (a = 6.3296 Å) and the anionic composition. The inset illustrates the cubic perovskite structure of $Cs_xFA_{1-x}Pb(Br_{1-y}I_y)_3$ NCs (space group $Pm\bar{3}m$, with y = 0.87 and x = 0), in which the perovskite framework consists of PbX_6 units sharing the octahedral corners; the X^- anions are disordered in four equivalent positions.

flask reactors, we carried out hot-injection synthesis of both $Cs_xFA_{1-x}PbI_3$ and $Cs_xFA_{1-x}Pb(Br_{1-y}I_y)_3$ NCs (further details are provided in the Methods section). Briefly, to synthesize NCs with the nominal composition of $Cs_{0.01}FA_{0.99}Pb(Br_{0.11}I_{0.89})_3$ (Figure 5), PbI_2 (55 mg, 0.12 mmol) and $PbBr_2$ (5 mg, 0.014 mmol) were suspended in 1-octadecene (ODE, 4.6 mL), heated to 60 °C, and then dried under vacuum for 30 min. Subsequently, the reaction mixture was heated to 110 °C in a nitrogen environment, followed by the addition of dried solvents: oleylamine (OLA, 0.5 mL) and oleic acid (OA, 1.0 mL). Once the PbI_2 dissolved, the reaction mixture was cooled to 80 °C. At this point, a mixture of FA oleate (4.8 mL) and Cs oleate (1.2 mL) stock solutions was injected into the reaction flask. After 5 s, the reaction was quenched. The crude solution was then centrifuged and the supernatant was discarded. The precipitate was dissolved in hexane, and the resulting solution was centrifuged once again, after which the supernatant and precipitate were separated. The particles from both fractions, supernatant and precipitate, were further washed to remove excess organic ligands (see further details in the Methods section). This synthesis procedure yielded nearly cubic NCs with a PL peak at 730 nm (Figure 5a−c), a PL fwhm of 40 nm (after isolation and purification), and a PL quantum yield (QY) of 80−89%. QY drops to *ca.* 50% in the solid-state form (NC film). We note that the larger fwhm values detected in-line in microfluidics can be attributed to size-fractioning that occurs during isolation and purification.

Crystal Structure. To uncover the structural details of $Cs_xFA_{1-x}Pb(Br_{1-y}I_y)_3$ NCs, synchrotron X-ray total scattering measurements were performed (using an octane solution of NCs in a quartz capillary, Figure 5c) at the X04SA-MS4 Powder Diffraction Beamline of the Swiss Light Source (Paul Scherrer Institute, Villigen, CH).[120] A combined Rietveld and total scattering approach based on the Debye scattering equation (DSE, accounting for structure, size, and anisotropic morphology)[121] was used for structural and microstructural characterization of $Cs_xFA_{1-x}Pb(Br_{1-y}I_y)_3$ NCs (details are provided in the Supporting Information). The analysis results suggest a cubic structure in which X^- anions are disordered in four equivalent sites around the equilibrium position (inset of Figure 5c), similar to the disorder seen in $FAPbI_3$ and $FAPbBr_3$ NCs.[69,122] The atomic displacement parameters (in the form of the Debye−Waller factor) were refined for all atoms; the anomalously high values for halides in the unsplit cubic arrangement suggest local structural disorder. The graphical outcomes of the DSE-based analysis of $Cs_xFA_{1-x}Pb(Br_{1-y}I_y)_3$ NCs are summarized in Figures 5c, S13, and S14. In a similar manner to $CsPbX_3$ NCs,[12] the peak positions slightly deviate from the cubic metric. Nevertheless, the hybrid NCs investigated here exhibited a different kind of structural defectiveness, which needs further investigation.

DOI: 10.1021/acsnano.8b01122
ACS Nano 2018, 12, 5504−5517

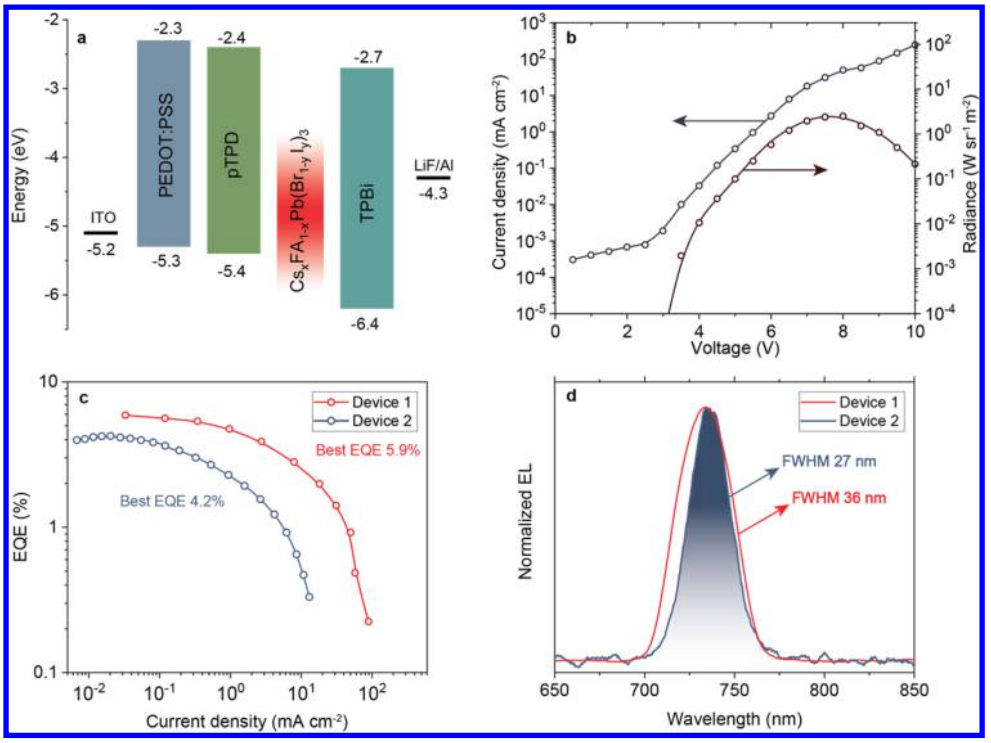

Figure 6. (a) Energy diagram of LED devices with $Cs_xFA_{1-x}Pb(Br_{1-y}I_y)_3$ NCs as emissive layers. (b) Current density and radiance *versus* voltage characteristics of device 1. (c) External quantum efficiency *versus* current density characteristics shown for devices 1 and 2. (d) Narrowest EL spectra of device 1 and device 2.

In addition, to further validate our findings, we compared the experimental data with a *Pnma* orthorhombic structure model (Figure S15).[123] The *Pnma* structure does not reproduce the experimental peak intensities; at the same time, new peaks appear in a simulation, without having a counterpart in the experimental data, thus supporting the analysis presented in Figure 5c. To investigate the substitutional disorder between the FA_{1-x}/Cs_x and Br_{1-y}/I_y couples, the corresponding site occupancy factors (s.o.f.) were refined by the conventional Rietveld method, and the resulting values ($x = 0$; $y = 0.87$) were kept fixed during DSE-based modeling. The Br/I substitution value is consistent with the PL peak position and with that estimated by X-ray fluorescence (XRF). The Cs quantity was too low to be detected by X-ray techniques; however, a small quantity of this cation (<5%) might be present in the crystal structure. Concerning the *structurally refined* s.o.f. value of Br (0.13), an even more robust determination (s.o.f = 0.10) was *independently* derived by adopting Vegard's law, which correlates the refined lattice parameter and anionic composition of the mixed halide, $Cs_xFA_{1-x}Pb(Br_{1-y}I_y)_3$ (for $x \approx 0$ and $a = 6.3296$ Å), with the two end members of the same series ($FAPbI_3$, $a = 6.3639$ Å, and $FAPbBr_3$, $a = 6.0042$ Å),[69,122] as depicted in Figure S14. Additionally, using a standard benchtop energy dispersive XRF instrument and a calibration mixture of $Pb(NO_3)_2$ and KBr in a 5:1 ratio, the Br fraction in the title compound was calculated to be 0.16(3), corroborating the presented estimates. In addition, to assess whether the quinary compositions undergo phase separation into respective ternary compounds, we report the pattern of a mixture of $FAPbBr_3$ (13% w/w) and $FAPbI_3$ (87% w/w) cubic phases and compare it to a solid solution model (Figure S16). The result indicates the absence of phase segregation. Overall, we highlight that FA^+ cations, fully or nearly fully occupying the A-site of the 3D perovskite framework, systematically favor the formation of a cubic structure [$FAPbI_3$, $FAPbBr_3$, and the herein studied $Cs_xFA_{1-x}Pb(Br_{1-y}I_y)_3$], whereas in $CsPbX_3$ NCs, the smaller Cs ions favor the tilting of octahedra and the formation of orthorhombic γ-phases, even after incorporation of up to 10% FA.[69]

Thermal stability of quinary NCs and, for comparison, $FAPbI_3$ NCs was evaluated using thermogravimetry and differential scanning calorimetry (DSC); see Figure S17. The decomposition of both kinds of NCs occurs in a few steps. Both show a most pronounced DSC feature at 335 °C that can be attributed to the decomposition of FA cations, indicating that both materials are of similar thermal stability.

Light-Emitting Diodes. $Cs_xFA_{1-x}Pb(Br_{1-y}I_y)_3$ NCs were used to construct LEDs with the device structure depicted in Figure 6a. These LEDs were fabricated by spin coating poly(3,4-ethylenedioxythiophene)-poly(styrenesulfonate) (PEDOT:PSS) on prepatterned indium tin oxide (ITO)-covered glass substrates, followed by the spin coating of poly(*N,N′*-bis(4-butylphenyl)-*N,N′*-bisphenylbenzidine (poly-TPD) and an NC emissive layer. Later, 50 nm of 2,2,2″-(1,3,5-benzinetriyl)tris(1-phenyl-1*H*-benzimidazole) (TPBi), 1.2 nm of lithium fluoride (LiF), and 100 nm of aluminum (Al) were sequentially evaporated on top of the emissive layer. Two different devices (1 and 2) were tested, with device 2 containing TOPAS polymer in the NC layer (TOPAS = cyclic olefin copolymer from TOPAS Advanced Polymers GmbH). LED performance was characterized by measuring current density and radiance as a function of the voltage applied between the ITO anode and Al cathode (Figure 6b) and by measuring the electroluminescence (EL) spectrum (Figure 6d). The current density of device 1 steadily increased from 8×10^{-4} mA cm^{-2} at 2 V to over 100 mA cm^{-2} at 10 V. The radiance surpassed 10^{-4} W sr^{-1} m^{-2} at just above 3 V and increased up to 3.9 W sr^{-1} m^{-2} at 7.5 V. The radiance, current density, and EL spectrum were then used to calculate the EQE, which describes the number of out-coupled photons per number of injected electrons. The EQE dependence on current density is shown in

DOI: 10.1021/acsnano.8b01122
ACS Nano 2018, 12, 5504−5517

Figure 6c, with a device 1 peak EQE of 5.9% at 0.1 mA cm^{-2} (0.2% at 100 mA cm^{-2}) and a device 2 peak EQE of 4.2%. The peak EQE and turn-on voltage of >3 V are in line with our previous work, in which we investigated $FAPbI_3$ LEDs emitting at 772 nm.[69] However, in the case of LEDs incorporating $Cs_xFA_{1-x}Pb(Br_{1-y}I_y)_3$ NCs, the EQE stays above 2.5% for currents up to 10 mA cm^{-2}. The peak radiance is also higher with quinary NCs (3.9 *versus* 1.54 W sr^{-1} m^{-2}).[69] While the low efficiency roll-off below 10 mA cm^{-2} indicates a good electron–hole balance in the emission layer[124] and excellent carrier/exciton confinement,[125] the turn-on voltage of over 3 V, ~1.3 V higher than expected from the band-gap energy of the $Cs_xFA_{1-x}Pb(Br_{1-y}I_y)_3$ NCs (~1.7 eV), suggests that further optimization of the device architecture is needed in order to reduce the charge-injection barrier(s). The EL spectra (Figure 6d) revealed a sharp peak near 735 nm with a narrowest fwhm of 37 nm at 9 V for device 1 and as low as 27 nm at 8.5 V for device 2. Figures S18 and S19 present the evolution of EL spectra with increasing the voltage, for both devices. Even though device 1 showed the best EQE value of 5.9% and peak radiance of 3.9 W sr^{-1} m^{-2}, device 2 (best EQE of 4.2%) showed a distinctly different behavior: EL peak narrowing at higher voltages (Figure S19), from an initial fwhm of 40 nm to 27 nm at 8.5 V. In device 2, the fwhm of the EL spectrum is strikingly narrower than that in the NC PL spectra in the solution (fwhm = 40 nm) and in films (fwhm = 52 nm); see Figure S20 for comparison. Together with the red shift of the EL peak position, this might indicate an efficient energy transfer between the NCs.[126] As a plausible scenario, the applied voltage might induce anion migration and hence alter the energy band gaps of NCs within the layer.[127] The emission might then occur through the channeling of excitation into the specific population of NCs. To the best of our knowledge, the EL fwhm of 27 nm (62 meV) is the narrowest among those reported for the red (and near-IR) perovskite LEDs. Figure S21 shows typical transient properties of the NC LED at a constant voltage of 4.5 V. Significant growth of the current density from 0.1 mA cm^{-2} to over 5 mA cm^{-2} within seconds is observed. This might again support the possibility of the ionic rearrangement within the NC film that improves charge injection, similar to the light-emitting electrochemical devices.[128] The overall LED device lifetime (to reach half of the maximum EL intensity) at 4.5 V bias is about half a minute. For comparison, other perovskite LEDs in this wavelength range are those utilizing methylammonium lead iodide ($MAPbI_3$) thin films treated with *n*-butylammonium iodide (EQE of 10.4%),[129] quasi-2D perovskites (EQE of 8.8%),[126] and multiple quantum wells (EQE of 11.7%).[130]

CONCLUSIONS

Herein, we have described the combinatorial synthesis of highly luminescent and stable $Cs_xFA_{1-x}Pb(Br_{1-y}I_y)_3$ NCs with emission and absorption spectra between 690 and 780 nm. Using a microfluidic platform, we identified the compositional parametric zones for fine-tuning optical properties, while retaining emission line widths in the range of 45–65 nm (before isolation, size selection, and purification). Importantly, microfluidic parameters can be readily transferred to conventional flask-based synthetic processes used by the perovskite research community. The PL fwhm can be further refined to ~40 nm as a result of the size selection occurring during the isolation and purification of NCs. Characterization by synchrotron X-ray scattering indicates a cubic structure for the $Cs_xFA_{1-x}Pb(Br_{1-y}I_y)_3$ NCs, wherein solid mixed-anion solutions can be clearly confirmed. The distribution of Cs ions remains rather controversial, yet its addition to the reaction mixture is of paramount importance in improving the long-term stability of NCs. The successful fabrication of NC-based LED devices with EQEs as high as 5.9% indicates the excellent chemical durability of $Cs_xFA_{1-x}Pb(Br_{1-y}I_y)_3$ NCs. Future studies should focus on understanding the interesting observations of the slow transient response of the LEDs and narrow EL spectral line width of 27 at 735 nm.

The synthesis of multinary lead halide perovskite (LHP) NCs might open opportunities for the broad deployment of these nanomaterials in photovoltaics and other optoelectronic devices. For instance, these infrared-active NCs are highly desirable for applications in single-junction or tandem photovoltaics, where NC colloids can be employed as inks for depositing active absorbing layers.[1,17] In this regard, in contrast to conventional molecular LHP solutions used as inks, the ease of compositional engineering and facile ligand removal exhibited by the currently developed quinary NCs, followed by low-temperature sintering for recrystallization into continuous thin films, suggests numerous possibilities. Alternatively, or rather orthogonally, methods of surface coating for maintaining the quantum-size effects may enable thin-film or quantum-dot-like photovoltaic devices[17,131] and photodetectors.[132]

METHODS

Materials. Cesium carbonate (Cs_2CO_3, Aldrich, 99.9%), formamidinium acetate (Sigma-Aldrich, 99.9%), lead bromide ($PbBr_2$, ABCR, 98%), lead iodide (PbI_2, ABCR, 99.999%), 1-octadecene (90%), oleic acid (Sigma-Aldrich, 90%), and oleylamine (Acros, ≥ 96%) were used as the reagents. Galden PFPE fluid was purchased from Blaser Swisslube AG. Patterned indium tin oxide (ITO)-covered glass substrates were purchased from Lumtech. The hole injection material PEDOT:PSS was purchased from Heraeus (CLEVIOS VP AI 4083), while the hole transport material poly-TPD was procured from Lumtech and the electron transport material TPBi was supplied by e-Ray Optoelectronics. The electron injection material LiF was purchased from Acros Organics, and Al pellets were purchased from Kurt J. Lesker Co. Ltd. TOPAS polymer (cyclic olefin copolymer) was received from TOPAS Advanced Polymers GmbH. All the materials for LED production were used as received without any further purification.

Microfluidic Synthesis. Various concentrations of precursor solutions (see Supporting Information for details) were used depending on the experimental purpose (sample collection, absorption measurements, PL measurements). Precision syringe pumps (neMESYS, Cetoni GmbH, Germany) were used to inject the dispersed phase (PbX_2, FA-oleate, and Cs-oleate precursor solutions) and the carrier fluid (Galden fluorinated fluid, Blaser Swisslube AG, Germany) toward a manifold (Manifold Assay 7 Port 10-32 Std, Upchurch Scientific, Germany) to form a segmented flow of droplets. The injection manifold and the syringes carrying the precursor solutions were connected through polytetrafluoroethylene tubing (i.d. 250 μm, o.d. 1/16 in., Upchurch Scientific, Germany) using polyether ether ketone finger-tight fittings (F-127, Upchurch Scientific, Germany). The carrier fluid was transferred to the manifold *via* fluorinated ethylene propylene tubing (i.d. 750 μm, o.d. 1/16 in., Upchurch Scientific, Germany). Typical flow rates were between 80 and 100 μL min^{-1} for the carrier phase and between 0.1 and 50 μL min^{-1} for the precursors. The chemical payload of the formed droplets can be tuned in a precise and rapid fashion by continuously varying the precursor volumetric flow rates. The formed droplets containing the reaction mixture were subsequently directed through perfluoroether tubing (i.d. 500 μm, o.d. 1/16 in., Upchurch Scientific, Germany) coiled around a copper heating rod (diameter = 1.5 cm) to allow initiation of the NC-forming reaction and online detection of the formed perovskite NCs. The overall reaction time was kept constant in all experiments by ensuring a

DOI: 10.1021/acsnano.8b01122
ACS Nano 2018, 12, 5504–5517

constant tubing length between the point where the tubing enters the heating rod and the detection volume.

Online Photoluminescence Measurements. A 375 nm LED (M375L3-Mounted LED, Thorlabs, Germany) was used as an excitation source for PL measurements. The collimated beam was directed toward a dichroic beam splitter (Multiphoton LP-Strahlenteiler HC 375 LP, AHF, Germany) and then focused into the microfluidic channel using an aspheric lens (A240TM, f = 8.0 mm, NA 0.50, Thorlabs, Germany). Emission originating from the microfluidic channel was collected by the same lens, passed through the dichroic beam splitter, and coupled *via* a 10× objective (RMS10X, NA 0.25, Thorlabs, Germany) to a fiber spectrometer (QE 65000, Ocean Optics, UK) *via* a 2 m long multimode fiber with a core diameter of 400 μm (QP400-2-UV−vis, Ocean Optics, UK). The spectrometer incorporated a 20 μm entrance slit, a 600 lines/mm grating, and a 2048-pixel detector. The spectrometer was operated between 350 and 1100 nm, and data were recorded using an integration time between 50 and 100 ms.

Online Absorbance Measurements. Absorbance measurements were conducted after the heating stage, where the reaction mixture flows through a high-purity perfluoralkoxy capillary (1/16 in. o.d., 500 μm i.d., IDEX Health & Science, USA). The in-line absorbance spectrometer consists of a fiber-coupled halogen lamp (HL-2000 HP, Ocean Optics, UK) and a fiber-coupled spectrometer (AvaSpec ULS2048 Starline, Avantes, USA). The spectrometer was operated between 200 and 1100 nm, and data were recorded using an integration time of 100 ms.

Flask Synthesis: Preparation of Formamidinium Oleate Stock Solution. Formamidinium acetate (3.765 mmol, 0.392 g, Aldrich, 99%) was loaded into a 50 mL three-neck flask along with ODE (18 mL) and OA (12 mL). The reaction mixture was degassed three times at room temperature, heated to 100 °C in a nitrogen environment, maintained at that temperature until the reaction is complete, and then cooled to room temperature. The resulting solution was stored in a glovebox.

Flask Synthesis: Preparation of a Cesium Oleate Stock Solution. Cesium carbonate (0.015 mmol, 5 mg) was loaded into a 25 mL three-neck flask along with ODE (10 mL) and OA (0.625 mL). The reaction mixture was degassed three times at room temperature, heated to 120 °C in a nitrogen atmosphere, maintained at that temperature until the reaction was complete, and cooled to room temperature. The resulting solution was stored in a glovebox.

Flask Synthesis of $Cs_{0.01}FA_{0.99}Pb(Br_{0.11}I_{0.89})_3$ NCs. In a 25 mL three-necked flask, PbI_2 (55 mg, 0.12 mmol, Sigma-Aldrich) and $PbBr_2$ (5 mg, 0.014 mmol, Sigma-Aldrich) were suspended in ODE (4.6 mL), heated to 60 °C, and then dried under vacuum for 30 min. Subsequently, the reaction mixture was heated to 110 °C in a nitrogen atmosphere, followed by the addition of dried solvents: OLA (0.5 mL, Strem) and OA (1.0 mL, Aldrich). Once PbI_2 was dissolved, the reaction mixture was cooled to 80 °C. At this point, a mixture of the formamidinium oleate (4.8 mL) and cesium oleate (1.2 mL) stock solutions was injected into the reaction flask. After another 15 s, the reaction mixture was cooled using a water-ice bath. The crude solution was centrifuged at 12 100 rpm for 7 min, and the supernatant discarded. The precipitate was dissolved in hexane (250 μL), and the resulting solution was centrifuged again at 10 000 rpm for 3 min. The supernatant and precipitate were separated, and 150 μL of hexane was added to the supernatant. This fraction was labeled as "SN". The precipitate was dissolved in toluene (1.0 mL) and centrifuged at 3500 rpm for 2 min to get rid of large NCs, with the resultant sample being labeled as "P". Particles from both fractions were washed again to remove excess organic ligands.

Washing of $Cs_{0.01}FA_{0.99}Pb(Br_{0.11}I_{0.89})_3$ SN NCs. To 100 μL of a hexane solution of NCs were added hexane (100 μL), toluene (200 μL), and methyl acetate (530 μL). The solution was centrifuged at 13 400 rpm for 3 min and redissolved in hexane or toluene (PL at ∼730 nm).

Washing of $Cs_{0.01}FA_{0.99}Pb(Br_{0.11}I_{0.89})_3$ P NCs. Methyl acetate (0.65 mL) was added to a toluene solution of fraction "P" and centrifuged for 3 min at 10 000 rpm. The obtained precipitate was dissolved in toluene, hexane, or octane (PL at ∼750 nm).

Offline Characterization. Ultraviolet−visible (UV−vis) absorbance spectra were recorded using a Jasco V770 spectrometer in transmission mode. Photoluminescence spectra were recorded using a Fluoromax iHR 320 Horiba Jobin Yvon spectrofluorimeter equipped with a PMT detector. The excitation wavelength was 400 nm, and the excitation source was a 450 W xenon lamp. The measured intensities were corrected to account for the spectral response of the detector. Powder XRD patterns were recorded using a powder diffractometer (STOE STADI P) with Cu Kα1 radiation. The diffractometer was operated in transmission mode with a germanium monochromator and a silicon strip detector (Dectris Mythen). TEM images were captured using a JEOL JEM-2200FS microscope operated at 200 kV. Quantitative XRF measurements were conducted using a benchtop Minipal 2 PANalytical spectrometer with polycarbonate films supporting dry colloids or powders and a Cr X-ray tube operating at a maximum power of 30 W. Thermal analysis (thermogravimetry and differential scanning calorimetry) was performed using a Netzsch Simultaneous thermal analyzer (STA 449 F5 Jupiter). A powdered sample (6−10 mg) was placed in an alumina crucible and heated under Ar gas flow (50 mL/min) to 800 °C (10 °C/min). NC solutions in hexane were predried in small alumina beakers at room temperature.

Quantum Yield Measurements. To measure the relative PL quantum yield of the NC solution, dilute solutions of NCs in toluene and dye standards (Rhodamine 6G in ethanol and zinc phthalocyanine in benzene) were prepared in 10 mm optical path length cuvettes, ensuring an absorbance of approximately 0.1 at either 488 or 633 nm. PL quantum yields were calculated according to

$$\Phi^i_f = \frac{F^i f_s n_i^2}{F^s f_i n_s^2}\Phi^s_f$$

where Φ^i_f and Φ^s_f are the PL QYs of the sample and standard, respectively; F^i and F^s are the integrated areas of the sample and standard spectra, respectively; f_i and f_s are the absorption factors of the sample and standard ($f = 1-10^{-A}$, where A is the absorbance), respectively; n_i and n_s are the refractive indices of the sample and standard, respectively.[133]

Absolute quantum yield measurements of the films and NC solutions were performed using a Hamamatsu Quantaurus QY spectrometer (C11347-11) equipped with an integrating sphere. The excitation peak wavelength was 450 nm.

Fabrication of LED Devices. Initially, ITO substrates were rinsed with a mixture of deionized water and detergent solution. Subsequently, substrates were sonicated for 20 min in acetone and isopropyl alcohol. To enhance wettability, substrates were treated with an oxygen plasma for 10 min. An aqueous solution of PEDOT:PSS was spin-coated at 4000 rpm for 30 s, after which the ITO substrates were annealed on a hot plate under ambient conditions for 30 min at 130 °C. Subsequently, they were transferred into a nitrogen-filled glovebox for the deposition of subsequent layers. Poly-TPD was spin coated at 1000 rpm from a 2 mg/mL chlorobenzene solution and annealed for 20 min at 120 °C. For device 1 a colloidal suspension of $Cs_xFA_{1-x}Pb(Br_{1-y}I_y)_3$ NCs in hexane (7 mg/mL) was spin coated at 2000 rpm; for device 2 the NC solution was mixed with TOPAS polymer (0.5 mg/mL) and spin coated at 2000 rpm. Subsequently, the substrates were transferred into a vacuum chamber at 10^{-7} mbar, where 50 nm of TPBi (electron transport layer), 1.2 nm of LiF, and 100 nm of Al (cathode) were evaporated through a shadow mask at evaporation rates of 0.5, 0.1, and 2 A/s, respectively. An active pixel area of 16 mm^2 was determined by the overlap of ITO and Al. All devices were measured under ambient conditions without encapsulation.

LED Performance Characterization. The $J-V-L$ characteristics of the fabricated LEDs were measured under ambient conditions using a Keysight 2902b source measurement unit and a calibrated photodiode (FDS1010-CAL, Thorlabs). The size of the photodiode (10 × 10 mm^2) is much larger than that of the active pixel size (4 × 4 mm^2) of the LEDs. The EQEs of the fabricated LEDs were calculated from the known EL spectra of the LEDs and photodiode sensitivity,[134] while the radiance was calculated assuming a Lambertian emission profile. EL spectra were recorded using a CCS200 CCD spectrometer (Thorlabs) and a PR-655 (Photoresearch) spectroradiometer. LED transient optoelectronic properties were measured with a Keysight 2902b source measurement unit and amplified photodiode (PDA36A-EC, Thorlabs) with 20 μs resolution.

DOI: 10.1021/acsnano.8b01122
ACS Nano 2018, 12, 5504−5517

Synchrotron X-ray Total Scattering Measurements. The experimental synchrotron X-ray total scattering data of colloidal $Cs_xFA_{1-x}(Br_{1-y}I_y)_3$ NCs (FA = $[HC(NH_2)_2]^+$) NCs in octane were collected at the X04SA-MS4 Powder Diffraction Beamline of the Swiss Light Source (Paul Scherrer Institute, Villigen, CH) using a certified quartz capillary (0.5 mm in diameter). The operational beam energy was set to 22 keV (λ = 0.563 729 Å) and accurately determined using a silicon powder standard (NIST 640d, a_0 = 0.543 123(8) nm at 22.5 °C). Data were collected in the 0.5−130° 2θ range using a single-photon-counting silicon microstrip detector (MYTHEN II). Total scattering patterns with air background, empty glass capillary, and pure solvent were independently collected under the same experimental conditions and properly subtracted from the sample signal. Transmission coefficients of the sample- and solvent-loaded capillaries were also measured and used for angle-dependent absorption correction. Inelastic Compton scattering was added as an additional model component during data analysis. For DSE-based modeling, an angular range of 3−120° was used.

Temperature-dependent measurements were also performed in the range of 98−348 K using a temperature-controlled N_2 stream fluxing over the capillary. No phase transitions were observed in the explored temperature range.

ASSOCIATED CONTENT

Supporting Information

The Supporting Information is available free of charge on the ACS Publications website at DOI: 10.1021/acsnano.8b01122.

Additional schematic illustration, preparation of precursors, synthesis procedure in a flask, TEM images, XRD patterns, and the PL and absorption spectra of $Cs_xFA_{1-x}PbX_3$ NCs (PDF)

AUTHOR INFORMATION

Corresponding Authors

*E-mail: maryna.bodnarchuk@empa.ch.
*E-mail: andrew.demello@chem.ethz.ch.
*E-mail: mvkovalenko@ethz.ch.

ORCID

Ioannis Lignos: 0000-0002-6816-3290
Richard M. Maceiczyk: 0000-0001-5735-2689
Loredana Protesescu: 0000-0002-9776-9881
Federica Bertolotti: 0000-0002-6001-9040
Sudhir Kumar: 0000-0002-2994-7084
Norberto Masciocchi: 0000-0001-9921-2350
Antonietta Guagliardi: 0000-0001-6390-2114
Chih-Jen Shih: 0000-0002-5258-3485
Andrew J. deMello: 0000-0003-1943-1356
Maksym V. Kovalenko: 0000-0002-6396-8938

Present Address

¶Department of Chemical Engineering, Massachusetts Institute of Technology, 77 Massachusetts Avenue, Cambridge, Massachusetts 02139, United States.

Notes

The authors declare no competing financial interest.

ACKNOWLEDGMENTS

This work was financially supported by the European Union through the FP7 grant (ERC Starting Grant NANOSOLID, GA No. 306733) and by the Swiss Federal Commission for Technology and Innovation (CTI-No. 18614.1 PFNM-NM). M.I.B. acknowledges financial support from the Swiss National Foundation (SNF Ambizione Energy Grant No. PZENP2_154287). F.B. acknowledges the European Union and Aarhus Institute of Advanced Studies (Aarhus University) for the Marie Skłodowska-Curie AIAS-COFUND grant (EU-FP7 program, Grant Agreement No. 609033). A.d.M. acknowledges partial support from a National Research Foundation (NRF) grant funded by the Ministry of Science, ICT and Future Planning of Korea, through the Global Research Laboratory Program (Grant No. 2009-00426). The technical staff of the X04SA-MS Beamline of the Swiss Light Source (PSI, Villigen, CH) are gratefully acknowledged. We further thank Ms. Franziska Krieg and Dr. Frank Krumeich for TEM imaging, Olga Nazarenko for TGA and DSC measurements, and Sergii Yakunin for absolute PL QY measurements.

REFERENCES

(1) Akkerman, Q. A.; Gandini, M.; Di Stasio, F.; Rastogi, P.; Palazon, F.; Bertoni, G.; Ball, J. M.; Prato, M.; Petrozza, A.; Manna, L. Strongly Emissive Perovskite Nanocrystal Inks for High-Voltage Solar Cells. *Nat. Energy* **2016**, *2*, 16194.

(2) Kim, H. S.; Lee, C. R.; Im, J. H.; Lee, K. B.; Moehl, T.; Marchioro, A.; Moon, S. J.; Humphry-Baker, R.; Yum, J. H.; Moser, J. E.; Gratzel, M.; Park, N. G. Lead Iodide Perovskite Sensitized All-Solid-State Submicron Thin Film Mesoscopic Solar Cell with Efficiency Exceeding 9%. *Sci. Rep.* **2012**, *2*, 591.

(3) Lee, M. M.; Teuscher, J.; Miyasaka, T.; Murakami, T. N.; Snaith, H. J. Efficient Hybrid Solar Cells Based on Meso-Superstructured Organometal Halide Perovskites. *Science* **2012**, *338*, 643−647.

(4) Saliba, M.; Matsui, T.; Domanski, K.; Seo, J. Y.; Ummadisingu, A.; Zakeeruddin, S. M.; Correa-Baena, J. P.; Tress, W. R.; Abate, A.; Hagfeldt, A.; Gratzel, M. Incorporation of Rubidium Cations into Perovskite Solar Cells Improves Photovoltaic Performance. *Science* **2016**, *354*, 206−209.

(5) Schmidt, L. C.; Pertegas, A.; Gonzalez-Carrero, S.; Malinkiewicz, O.; Agouram, S.; Espallargas, G. M.; Bolink, H. J.; Galian, R. E.; Perez-Prieto, J. Nontemplate Synthesis of $CH_3NH_3PbBr_3$ Perovskite Nanoparticles. *J. Am. Chem. Soc.* **2014**, *136*, 850−853.

(6) Protesescu, L.; Yakunin, S.; Bodnarchuk, M. I.; Krieg, F.; Caputo, R.; Hendon, C. H.; Yang, R. X.; Walsh, A.; Kovalenko, M. V. Nanocrystals of Cesium Lead Halide Perovskites ($CsPbX_3$, X = Cl, Br, and I): Novel Optoelectronic Materials Showing Bright Emission with Wide Color Gamut. *Nano Lett.* **2015**, *15*, 3692−3696.

(7) Zhang, F.; Zhong, H.; Chen, C.; Wu, X. G.; Hu, X.; Huang, H.; Han, J.; Zou, B.; Dong, Y. Brightly Luminescent and Color-Tunable Colloidal $CH_3NH_3PbX_3$ (X = Br, I, Cl) Quantum Dots: Potential Alternatives for Display Technology. *ACS Nano* **2015**, *9*, 4533−4542.

(8) Pan, J.; Sarmah, S. P.; Murali, B.; Dursun, I.; Peng, W.; Parida, M. R.; Liu, J.; Sinatra, L.; Alyami, N.; Zhao, C.; Alarousu, E.; Ng, T. K.; Ooi, B. S.; Bakr, O. M.; Mohammed, O. F. Air-Stable Surface-Passivated Perovskite Quantum Dots for Ultra-Robust, Single- and Two-Photon-Induced Amplified Spontaneous Emission. *J. Phys. Chem. Lett.* **2015**, *6*, 5027−5033.

(9) Wang, Y.; Li, X. M.; Song, J. Z.; Xiao, L.; Zeng, H. B.; Sun, H. D. All-Inorganic Colloidal Perovskite Quantum Dots: A New Class of Lasing Materials with Favorable Characteristics. *Adv. Mater.* **2015**, *27*, 7101−7108.

(10) Huang, H.; Polavarapu, L.; Sichert, J. A.; Susha, A. S.; Urban, A. S.; Rogach, A. L. Colloidal Lead Halide Perovskite Nanocrystals: Synthesis, Optical Properties and Applications. *NPG Asia Mater.* **2016**, *8*, e328.

(11) Speirs, M. J.; Balazs, D. M.; Dirin, D. N.; Kovalenko, M. V.; Loi, M. A. Increased Efficiency in pn-Junction PbS QD Solar Cells via NaHS Treatment of the p-Type Layer. *Appl. Phys. Lett.* **2017**, *110*, 103904.

(12) Bertolotti, F.; Protesescu, L.; Kovalenko, M. V.; Yakunin, S.; Cervellino, A.; Billinge, S. J. L.; Terban, M. W.; Pedersen, J. S.; Masciocchi, N.; Guagliardi, A. Coherent Nanotwins and Dynamic Disorder in Cesium Lead Halide Perovskite Nanocrystals. *ACS Nano* **2017**, *11*, 3819−3831.

(13) Sutherland, B. R.; Sargent, E. H. Perovskite Photonic Sources. *Nat. Photonics* **2016**, *10*, 295−302.

(14) Kim, Y. H.; Cho, H.; Lee, T. W. Metal Halide Perovskite Light Emitters. *Proc. Natl. Acad. Sci. U. S. A.* **2016**, *113*, 11694−11702.

DOI: 10.1021/acsnano.8b01122
ACS Nano 2018, 12, 5504−5517

(15) Li, X.; Cao, F.; Yu, D.; Chen, J.; Sun, Z.; Shen, Y.; Zhu, Y.; Wang, L.; Wei, Y.; Wu, Y.; Zeng, H. All Inorganic Halide Perovskites Nanosystem: Synthesis, Structural Features, Optical Properties and Optoelectronic Applications. *Small* **2017**, *13*, 1603996.
(16) Jia, Y.; Kerner, R. A.; Grede, A. J.; Rand, B. P.; Giebink, N. C. Continuous-Wave Lasing in an Organic–Inorganic Lead Halide Perovskite Semiconductor. *Nat. Photonics* **2017**, *11*, 784–788.
(17) Swarnkar, A.; Marshall, A. R.; Sanehira, E. M.; Chernomordik, B. D.; Moore, D. T.; Christians, J. A.; Chakrabarti, T.; Luther, J. M. Quantum Dot-Induced Phase Stabilization of alpha-$CsPbI_3$ Perovskite for High-Efficiency Photovoltaics. *Science* **2016**, *354*, 92–95.
(18) Kovalenko, M. V.; Manna, L.; Cabot, A.; Hens, Z.; Talapin, D. V.; Kagan, C. R.; Klimov, V. I.; Rogach, A. L.; Reiss, P.; Milliron, D. J.; Guyot-Sionnnest, P.; Konstantatos, G.; Parak, W. J.; Hyeon, T.; Korgel, B. A.; Murray, C. B.; Heiss, W. Prospects of Nanoscience with Nanocrystals. *ACS Nano* **2015**, *9*, 1012–1057.
(19) Chen, Z. H.; Li, H.; Tang, Y. B.; Huang, X.; Ho, D.; Lee, C. S. Shape-Controlled Synthesis of Organolead Halide Perovskite Nanocrystals and Their Tunable Optical Absorption. *Mater. Res. Express* **2014**, *1*, 015034.
(20) Hassan, Y.; Song, Y.; Pensack, R. D.; Abdelrahman, A. I.; Kobayashi, Y.; Winnik, M. A.; Scholes, G. D. Structure-Tuned Lead Halide Perovskite Nanocrystals. *Adv. Mater.* **2016**, *28*, 566–573.
(21) Jang, D. M.; Park, K.; Kim, D. H.; Park, J.; Shojaei, F.; Kang, H. S.; Ahn, J. P.; Lee, J. W.; Song, J. K. Reversible Halide Exchange Reaction of Organometal Trihalide Perovskite Colloidal Nanocrystals for Full-Range Band Gap Tuning. *Nano Lett.* **2015**, *15*, 5191–5199.
(22) Vybornyi, O.; Yakunin, S.; Kovalenko, M. V. Polar-Solvent-Free Colloidal Synthesis of Highly Luminescent Alkylammonium Lead Halide Perovskite Nanocrystals. *Nanoscale* **2016**, *8*, 6278–6283.
(23) Zhu, F.; Men, L.; Guo, Y. J.; Zhu, Q. C.; Bhattacharjee, U.; Goodwin, P. M.; Petrich, J. W.; Smith, E. A.; Vela, J. Shape Evolution and Single Particle Luminescence of Organometal Halide Perovskite Nanocrystals. *ACS Nano* **2015**, *9*, 2948–2959.
(24) Wang, Z.; Shi, Z.; Li, T.; Chen, Y.; Huang, W. Stability of Perovskite Solar Cells: A Prospective on the Substitution of the A Cation and X Anion. *Angew. Chem., Int. Ed.* **2017**, *56*, 1190–1212.
(25) Hoke, E. T.; Slotcavage, D. J.; Dohner, E. R.; Bowring, A. R.; Karunadasa, H. I.; McGehee, M. D. Reversible photo-induced trap formation in mixed-halide hybrid perovskites for photovoltaics. *Chem. Sci.* **2015**, *6*, 613–617.
(26) Akkerman, Q. A.; D'Innocenzo, V.; Accornero, S.; Scarpellini, A.; Petrozza, A.; Prato, M.; Manna, L. Tuning the Optical Properties of Cesium Lead Halide Perovskite Nanocrystals by Anion Exchange Reactions. *J. Am. Chem. Soc.* **2015**, *137*, 10276–10281.
(27) Akkerman, Q. A.; Motti, S. G.; Kandada, A. R. S.; Mosconi, E.; D'Innocenzo, V.; Bertoni, G.; Marras, S.; Kamino, B. A.; Miranda, L.; De Angelis, F.; Petrozza, A.; Prato, M.; Manna, L. Solution Synthesis Approach to Colloidal Cesium Lead Halide Perovskite Nanoplatelets with Monolayer-Level Thickness Control. *J. Am. Chem. Soc.* **2016**, *138*, 1010–1016.
(28) Bekenstein, Y.; Koscher, B. A.; Eaton, S. W.; Yang, P. D.; Alivisatos, A. P. Highly Luminescent Colloidal Nanoplates of Perovskite Cesium Lead Halide and Their Oriented Assemblies. *J. Am. Chem. Soc.* **2015**, *137*, 16008–16011.
(29) Chen, X.; Peng, L. C.; Huang, K. K.; Shi, Z.; Xie, R. G.; Yang, W. S. Non-Injection Gram-Scale Synthesis of Cesium Lead Halide Perovskite Quantum Dots with Controllable Size and Composition. *Nano Res.* **2016**, *9*, 1994–2006.
(30) Koolyk, M.; Amgar, D.; Aharon, S.; Etgar, L. Kinetics of Cesium Lead Halide Perovskite Nanoparticle Growth; Focusing and De-Focusing of Size Distribution. *Nanoscale* **2016**, *8*, 6403–6409.
(31) Nedelcu, G.; Protesescu, L.; Yakunin, S.; Bodnarchuk, M. I.; Grotevent, M. J.; Kovalenko, M. V. Fast Anion-Exchange in Highly Luminescent Nanocrystals of Cesium Lead Halide Perovskites ($CsPbX_3$, X = Cl, Br, I). *Nano Lett.* **2015**, *15*, 5635–5640.
(32) Palazon, F.; Akkerman, Q. A.; Prato, M.; Manna, L. X-ray Lithography on Perovskite Nanocrystals Films: From Patterning with Anion-Exchange Reactions to Enhanced Stability in Air and Water. *ACS Nano* **2016**, *10*, 1224–1230.
(33) Ramasamy, P.; Lim, D. H.; Kim, B.; Lee, S. H.; Lee, M. S.; Lee, J. S. All-Inorganic Cesium Lead Halide Perovskite Nanocrystals for Photodetector Applications. *Chem. Commun.* **2016**, *52*, 2067–2070.
(34) Shamsi, J.; Dang, Z. Y.; Bianchini, P.; Canale, C.; Di Stasio, F.; Brescia, R.; Prato, M.; Manna, L. Colloidal Synthesis of Quantum Confined Single Crystal $CsPbBr_3$ Nanosheets with Lateral Size Control up to the Micrometer Range. *J. Am. Chem. Soc.* **2016**, *138*, 7240–7243.
(35) Sun, S. B.; Yuan, D.; Xu, Y.; Wang, A. F.; Deng, Z. T. Ligand-Mediated Synthesis of Shape-Controlled Cesium Lead Halide Perovskite Nanocrystals via Reprecipitation Process at Room Temperature. *ACS Nano* **2016**, *10*, 3648–3657.
(36) Tong, Y.; Bladt, E.; Ayguler, M. F.; Manzi, A.; Milowska, K. Z.; Hintermayr, V. A.; Docampo, P.; Bals, S.; Urban, A. S.; Polavarapu, L.; Feldmann, J. Highly Luminescent Cesium Lead Halide Perovskite Nanocrystals with Tunable Composition and Thickness by Ultrasonication. *Angew. Chem., Int. Ed.* **2016**, *55*, 13887–13892.
(37) Yassitepe, E.; Yang, Z. Y.; Voznyy, O.; Kim, Y.; Walters, G.; Castaeda, J. A.; Kanjanaboos, P.; Yuan, M. J.; Gong, X. W.; Fan, F. J.; Pan, J.; Hoogland, S.; Comin, R.; Bakr, O. M.; Padilha, L. A.; Nogueira, A. F.; Sargent, E. H. Amine-Free Synthesis of Cesium Lead Halide Perovskite Quantum Dots for Efficient Light-Emitting Diodes. *Adv. Funct. Mater.* **2016**, *26*, 8757–8763.
(38) Imran, M.; Di Stasio, F.; Dang, Z.; Canale, C.; Khan, A. H.; Shamsi, J.; Brescia, R.; Prato, M.; Manna, L. Colloidal Synthesis of Strongly Fluorescent $CsPbBr_3$ Nanowires with Width Tunable down to the Quantum Confinement Regime. *Chem. Mater.* **2016**, *28*, 6450–6454.
(39) Levchuk, I.; Osvet, A.; Tang, X.; Brandl, M.; Perea, J. D.; Hoegl, F.; Matt, G. J.; Hock, R.; Batentschuk, M.; Brabec, C. J. Brightly Luminescent and Color-Tunable Formamidinium Lead Halide Perovskite $FAPbX_3$ (X = Cl, Br, I) Colloidal Nanocrystals. *Nano Lett.* **2017**, *17*, 2765–2770.
(40) Imran, M.; Caligiuri, V.; Wang, M.; Goldoni, L.; Prato, M.; Krahne, R.; De Trizio, L.; Manna, L. Benzoyl Halides as Alternative Precursors for the Colloidal Synthesis of Lead-Based Halide Perovskite Nanocrystals. *J. Am. Chem. Soc.* **2018**, *140*, 2656–2664.
(41) Krieg, F.; Ochsenbein, S. T.; Yakunin, S.; ten Brinck, S.; Aellen, P.; Süess, A.; Clerc, B.; Guggisberg, D.; Nazarenko, O.; Shynkarenko, Y.; Kumar, S.; Shih, C.-J.; Infante, I.; Kovalenko, M. V. Colloidal $CsPbX_3$ (X = Cl, Br, I) Nanocrystals 2.0: Zwitterionic Capping Ligands for Improved Durability and Stability. *ACS Energy Lett.* **2018**, *3*, 641–646.
(42) Zhang, D. D.; Eaton, S. W.; Yu, Y.; Dou, L. T.; Yang, P. D. Solution-Phase Synthesis of Cesium Lead Halide Perovskite Nanowires. *J. Am. Chem. Soc.* **2015**, *137*, 9230–9233.
(43) Zhang, D. D.; Yang, Y. M.; Bekenstein, Y.; Yu, Y.; Gibson, N. A.; Wong, A. B.; Eaton, S. W.; Kornienko, N.; Kong, Q.; Lai, M. L.; Alivisatos, A. P.; Leone, S. R.; Yang, P. D. Synthesis of Composition Tunable and Highly Luminescent Cesium Lead Halide Nanowires through Anion-Exchange Reactions. *J. Am. Chem. Soc.* **2016**, *138*, 7236–7239.
(44) Zhang, D. D.; Yu, Y.; Bekenstein, Y.; Wong, A. B.; Alivisatos, A. P.; Yang, P. D. Ultrathin Colloidal Cesium Lead Halide Perovskite Nanowires. *J. Am. Chem. Soc.* **2016**, *138*, 13155–13158.
(45) Zhang, X. F.; Lv, L. F.; Ji, L.; Guo, G. N.; Liu, L. M.; Han, D. D.; Wang, B. W.; Tu, Y. Q.; Hu, J. H.; Yang, D.; Dong, A. G. Self-Assembly of One-Dimensional Nanocrystal Superlattice Chains Mediated by Molecular Clusters. *J. Am. Chem. Soc.* **2016**, *138*, 3290–3293.
(46) De Roo, J.; Ibanez, M.; Geiregat, P.; Nedelcu, G.; Walravens, W.; Maes, J.; Martins, J. C.; Van Driessche, I.; Koyalenko, M. V.; Hens, Z. Highly Dynamic Ligand Binding and Light Absorption Coefficient of Cesium Lead Bromide Perovskite Nanocrystals. *ACS Nano* **2016**, *10*, 2071–2081.
(47) Guo, Y. L.; Shoyama, K.; Sato, W.; Nakamura, E. Polymer Stabilization of Lead(II) Perovskite Cubic Nanocrystals for Semitransparent Solar Cells. *Adv. Energy Mater.* **2016**, *6*, 1502317.
(48) Huang, H.; Chen, B. K.; Wang, Z. G.; Hung, T. F.; Susha, A. S.; Zhong, H. Z.; Rogach, A. L. Water Resistant $CsPbX_3$ Nanocrystals

DOI: 10.1021/acsnano.8b01122
ACS Nano 2018, 12, 5504–5517

Coated with Polyhedral Oligomeric Silsesquioxane and Their Use as Solid State Luminophores in All-Perovskite White Light-Emitting Devices. *Chem. Sci.* **2016**, *7*, 5699−5703.
(49) Kim, Y.; Yassitepe, E.; Voznyy, O.; Comin, R.; Walters, G.; Gong, X. W.; Kanjanaboos, P.; Nogueira, A. F.; Sargent, E. H. Efficient Luminescence from Perovskite Quantum Dot Solids. *ACS Appl. Mater. Interfaces* **2015**, *7*, 25007−25013.
(50) Pan, J.; Quan, L. N.; Zhao, Y.; Peng, W.; Murali, B.; Sarmah, S. P.; Yuan, M.; Sinatra, L.; Alyami, N. M.; Liu, J.; Yassitepe, E.; Yang, Z.; Voznyy, O.; Comin, R.; Hedhili, M. N.; Mohammed, O. F.; Lu, Z. H.; Kim, D. H.; Sargent, E. H.; Bakr, O. M. Highly Efficient Perovskite-Quantum-Dot Light-Emitting Diodes by Surface Engineering. *Adv. Mater.* **2016**, *28*, 8718−8725.
(51) Hu, F. R.; Yin, C. Y.; Zhang, H. C.; Sun, C.; Yu, W. W.; Zhang, C. F.; Wang, X. Y.; Zhang, Y.; Xiao, M. Slow Auger Recombination of Charged Excitons in Nonblinking Perovskite Nanocrystals without Spectral Diffusion. *Nano Lett.* **2016**, *16*, 6425−6430.
(52) Hu, F. R.; Zhang, H. C.; Sun, C.; Yin, C. Y.; Lv, B. H.; Zhang, C. F.; Yu, W. W.; Wang, X. Y.; Zhang, Y.; Xiao, M. Superior Optical Properties of Perovskite Nanocrystals as Single Photon Emitters. *ACS Nano* **2015**, *9*, 12410−12416.
(53) Makarov, N. S.; Guo, S. J.; Isaienko, O.; Liu, W. Y.; Robel, I.; Klimov, V. I. Spectral and Dynamical Properties of Single Excitons, Biexcitons, and Trions in Cesium-Lead-Halide Perovskite Quantum Dots. *Nano Lett.* **2016**, *16*, 2349−2362.
(54) Park, Y. S.; Guo, S. J.; Makarov, N. S.; Klimov, V. I. Room Temperature Single-Photon Emission from Individual Perovskite Quantum Dots. *ACS Nano* **2015**, *9*, 10386−10393.
(55) Raino, G.; Nedelcu, G.; Protesescu, L.; Bodnarchuk, M. I.; Kovalenko, M. V.; Mahrt, R. F.; Stoferle, T. Single Cesium Lead Halide Perovskite Nanocrystals at Low Temperature: Fast Single-Photon Emission, Reduced Blinking, and Exciton Fine Structure. *ACS Nano* **2016**, *10*, 2485−90.
(56) Swarnkar, A.; Chulliyil, R.; Ravi, V. K.; Irfanullah, M.; Chowdhury, A.; Nag, A. Colloidal $CsPbBr_3$ Perovskite Nanocrystals: Luminescence Beyond Traditional Quantum Dots. *Angew. Chem., Int. Ed.* **2015**, *54*, 15424−15428.
(57) Tian, Y. X.; Merdasa, A.; Peter, M.; Abdellah, M.; Zheng, K. B.; Ponseca, C. S.; Pullerits, T.; Yartsev, A.; Sundstrom, V.; Scheblykin, I. G. Giant Photoluminescence Blinking of Perovskite Nanocrystals Reveals Single-Trap Control of Luminescence. *Nano Lett.* **2015**, *15*, 1603−1608.
(58) Utzat, H.; Shulenberger, K. E.; Achorn, O. B.; Nasilowski, M.; Sinclair, T. S.; Bawendi, M. G. Probing Linewidths and Biexciton Quantum Yields of Single Cesium Lead Halide Nanocrystals in Solution. *Nano Lett.* **2017**, *17*, 6838−6846.
(59) Yakunin, S.; Protesescu, L.; Krieg, F.; Bodnarchuk, M. I.; Nedelcu, G.; Humer, M.; De Luca, G.; Fiebig, M.; Heiss, W.; Kovalenko, M. V. Low-Threshold Amplified Spontaneous Emission and Lasing From Colloidal Nanocrystals of Caesium Lead Halide Perovskites. *Nat. Commun.* **2015**, *6*, 8056.
(60) Bai, Z. L.; Zhong, H. Z. Halide Perovskite Quantum Dots: Potential Candidates for Display Technology. *Sci. Bull.* **2015**, *60*, 1622−1624.
(61) Wang, H. C.; Lin, S. Y.; Tang, A. C.; Singh, B. P.; Tong, H. C.; Chen, C. Y.; Lee, Y. C.; Tsai, T. L.; Liu, R. S. Mesoporous Silica Particles Integrated with All-Inorganic $CsPbBr_3$ Perovskite Quantum-Dot Nanocomposites (MP-PQDs) with High Stability and Wide Color Gamut Used for Backlight Display. *Angew. Chem., Int. Ed.* **2016**, *55*, 7924−7929.
(62) Zhang, X. J.; Wang, H. C.; Tang, A. C.; Lin, S. Y.; Tong, H. C.; Chen, C. Y.; Lee, Y. C.; Tsai, T. L.; Liu, R. S. Robust and Stable Narrow-Band Green Emitter: An Option for Advanced Wide-Color-Gamut Backlight Display. *Chem. Mater.* **2016**, *28*, 8493−8497.
(63) Chiba, T.; Hoshi, K.; Pu, Y. J.; Takeda, Y.; Hayashi, Y.; Ohisa, S.; Kawata, S.; Kido, J. High-Efficiency Perovskite Quantum-Dot Light-Emitting Devices by Effective Washing Process and Interfacial Energy Level Alignment. *ACS Appl. Mater. Interfaces* **2017**, *9*, 18054−18060.
(64) Li, G. R.; Rivarola, F. W. R.; Davis, N. J. L. K.; Bai, S.; Jellicoe, T. C.; de la Pena, F.; Hou, S. C.; Ducati, C.; Gao, F.; Friend, R. H.; Greenham, N. C.; Tan, Z. K. Highly Efficient Perovskite Nanocrystal Light-Emitting Diodes Enabled by a Universal Crosslinking Method. *Adv. Mater.* **2016**, *28*, 3528−3534.
(65) Li, X. M.; Wu, Y.; Zhang, S. L.; Cai, B.; Gu, Y.; Song, J. Z.; Zeng, H. B. $CsPbX_3$ Quantum Dots for Lighting and Displays: Room-Temperature Synthesis, Photoluminescence Superiorities, Underlying Origins and White Light-Emitting Diodes. *Adv. Funct. Mater.* **2016**, *26*, 2435−2445.
(66) Song, J. Z.; Li, J. H.; Li, X. M.; Xu, L. M.; Dong, Y. H.; Zeng, H. B. Quantum Dot Light-Emitting Diodes Based on Inorganic Perovskite Cesium Lead Halides ($CsPbX_3$). *Adv. Mater.* **2015**, *27*, 7162−7167.
(67) Zhang, X. Y.; Lin, H.; Huang, H.; Reckmeier, C.; Zhang, Y.; Choy, W. C. H.; Rogach, A. L. Enhancing the Brightness of Cesium Lead Halide Perovskite Nanocrystal Based Green Light-Emitting Devices through the Interface Engineering with Perfluorinated Ionomer. *Nano Lett.* **2016**, *16*, 1415−1420.
(68) Zhang, X. Y.; Sun, C.; Zhang, Y.; Wu, H.; Ji, C. Y.; Chuai, Y. H.; Wang, P.; Wen, S. P.; Zhang, C. F.; Yu, W. W. Bright Perovskite Nanocrystal Films for Efficient Light-Emitting Devices. *J. Phys. Chem. Lett.* **2016**, *7*, 4602−4610.
(69) Protesescu, L.; Yakunin, S.; Kumar, S.; Bar, J.; Bertolotti, F.; Masciocchi, N.; Guagliardi, A.; Grotevent, M.; Shorubalko, I.; Bodnarchuk, M. I.; Shih, C. J.; Kovalenko, M. V. Dismantling the "Red Wall" of Colloidal Perovskites: Highly Luminescent Formamidinium and Formamidinium-Cesium Lead Iodide Nanocrystals. *ACS Nano* **2017**, *11*, 3119−3134.
(70) Lee, J. W.; Kim, D. H.; Kim, H. S.; Seo, S. W.; Cho, S. M.; Park, N. G. Formamidinium and Cesium Hybridization for Photo- and Moisture-Stable Perovskite Solar Cell. *Adv. Energy Mater.* **2015**, *5*, 1501310.
(71) Yi, C. Y.; Luo, J. S.; Meloni, S.; Boziki, A.; Ashari-Astani, N.; Gratzel, C.; Zakeeruddin, S. M.; Rothlisberger, U.; Gratzel, M. Entropic Stabilization of Mixed A-cation ABX_3 Metal Halide Perovskites for High Performance Perovskite Solar Cells. *Energy Environ. Sci.* **2016**, *9*, 656−662.
(72) Li, Z.; Yang, M. J.; Park, J. S.; Wei, S. H.; Berry, J. J.; Zhu, K. Stabilizing Perovskite Structures by Tuning Tolerance Factor: Formation of Formamidinium and Cesium Lead Iodide Solid-State Alloys. *Chem. Mater.* **2016**, *28*, 284−292.
(73) McMeekin, D. P.; Sadoughi, G.; Rehman, W.; Eperon, G. E.; Saliba, M.; Horantner, M. T.; Haghighirad, A.; Sakai, N.; Korte, L.; Rech, B.; Johnston, M. B.; Herz, L. M.; Snaith, H. J. A Mixed-Cation Lead Mixed-Halide Perovskite Absorber for Tandem Solar Cells. *Science* **2016**, *351*, 151−155.
(74) Nazarenko, O.; Yakunin, S.; Morad, V.; Cherniukh, I.; Kovalenko, M. V. Single Crystals of Caesium Formamidinium Lead Halide Perovskites: Solution Growth and Gamma Dosimetry. *NPG Asia Mater.* **2017**, *9*, e373.
(75) Rehman, W.; McMeekin, D. P.; Patel, J. B.; Milot, R. L.; Johnston, M. B.; Snaith, H. J.; Herz, L. M. Photovoltaic Mixed-Cation Lead Mixed-Halide Perovskites: Links Between Crystallinity, Photo-Stability and Electronic Properties. *Energy Environ. Sci.* **2017**, *10*, 361−369.
(76) Stoumpos, C. C.; Malliakas, C. D.; Kanatzidis, M. G. Semiconducting Tin and Lead Iodide Perovskites with Organic Cations: Phase Transitions, High Mobilities, and Near-Infrared Photoluminescent Properties. *Inorg. Chem.* **2013**, *52*, 9019−9038.
(77) Lignos, I.; Stavrakis, S.; Nedelcu, G.; Protesescu, L.; Demello, A. J.; Kovalenko, M. V. Synthesis of Cesium Lead Halide Perovskite Nanocrystals in a Droplet-Based Microfluidic Platform: Fast Parametric Space Mapping. *Nano Lett.* **2016**, *16*, 1869−1877.
(78) Maceiczyk, R. M.; Dumbgen, K.; Lignos, I.; Protesescu, L.; Kovalenko, M. V.; deMello, A. J. Microfluidic Reactors Provide Preparative and Mechanistic Insights into the Synthesis of Formamidinium Lead Halide Perovskite Nanocrystals. *Chem. Mater.* **2017**, *29*, 8433−8439.
(79) Lignos, I.; Protesescu, L.; Emiroglu, D. B.; Maceiczyk, R.; Schneider, S.; Kovalenko, M. V.; deMello, A. J. Unveiling the Shape Evolution and Halide-Ion-Segregation in Blue-Emitting Formamidinium Lead Halide Perovskite Nanocrystals Using an Automated Microfluidic Platform. *Nano Lett.* **2018**, *18*, 1246−1252.

DOI: 10.1021/acsnano.8b01122
ACS Nano 2018, 12, 5504−5517

(80) Han, Q. F.; Bae, S. H.; Sun, P. Y.; Hsieh, Y. T.; Yang, Y.; Rim, Y. S.; Zhao, H. X.; Chen, Q.; Shi, W. Z.; Li, G.; Yang, Y. Single Crystal Formamidinium Lead Iodide (FAPbI3): Insight into the Structural, Optical, and Electrical Properties. *Adv. Mater.* **2016**, *28*, 2253−2258.
(81) Saidaminov, M. I.; Abdelhady, A. L.; Maculan, G.; Bakr, O. M. Retrograde Solubility of Formamidinium and Methylammonium Lead Halide Perovskites Enabling Rapid Single Crystal Growth. *Chem. Commun.* **2015**, *51*, 17658−17661.
(82) Saidaminov, M. I.; Abdelhady, A. L.; Murali, B.; Alarousu, E.; Burlakov, V. M.; Peng, W.; Dursun, I.; Wang, L. F.; He, Y.; Maculan, G.; Goriely, A.; Wu, T.; Mohammed, O. F.; Bakr, O. M. High-Quality Bulk Hybrid Perovskite Single Crystals within Minutes by Inverse Temperature Crystallization. *Nat. Commun.* **2015**, *6*, 7586.
(83) Sharma, S.; Weiden, N.; Weiss, A. Phase-Diagrams of Quasi-Binary Systems of the Type - ABX_3-$A'BX_3$; ABX_3-$AB'X_3$, and ABX_3-ABX'_3 X = Halogen. *Z. Phys. Chem.* **1992**, *175*, 63−80.
(84) Trots, D. M.; Myagkota, S. V. High-Temperature Structural Evolution of Caesium and Rubidium Triiodoplumbates. *J. Phys. Chem. Solids* **2008**, *69*, 2520−2526.
(85) Zhumekenov, A. A.; Saidaminov, M. I.; Haque, M. A.; Alarousu, E.; Sarmah, S. P.; Murali, B.; Dursun, I.; Miao, X. H.; Abdelhady, A. L.; Wu, T.; Mohammed, O. F.; Bakr, O. M. Formamidinium Lead Halide Perovskite Crystals with Unprecedented Long Carrier Dynamics and Diffusion Length. *ACS Energy Lett.* **2016**, *1*, 32−37.
(86) Eperon, G. E.; Paterno, G. M.; Sutton, R. J.; Zampetti, A.; Haghighirad, A. A.; Cacialli, F.; Snaith, H. J. Inorganic Caesium Lead Iodide Perovskite Solar Cells. *J. Mater. Chem. A* **2015**, *3*, 19688−19695.
(87) Fang, H. H.; Wang, F.; Adjokatse, S.; Zhao, N.; Loi, M. A. Photoluminescence Enhancement in Formamidinium Lead Iodide Thin Films. *Adv. Funct. Mater.* **2016**, *26*, 4653−4659.
(88) Ma, F. S.; Li, J. W.; Li, W. Z.; Lin, N.; Wang, L. D.; Qiao, J. Stable Alpha/Delta Phase Junction of Formamidinium Lead Iodide Perovskites for Enhanced Near-Infrared Emission. *Chem. Sci.* **2017**, *8*, 800−805.
(89) Filip, M. R.; Eperon, G. E.; Snaith, H. J.; Giustino, F. Steric Engineering of Metal-Halide Perovskites with Tunable Optical Band Gaps. *Nat. Commun.* **2014**, *5*, 5757.
(90) Goldschmidt, V. M. Die Gesetze der Krystallochemie. *Naturwissenschaften* **1926**, *14*, 477−485.
(91) Kieslich, G.; Sun, S.; Cheetham, A. K. Solid-State Principles Applied to Organic-Inorganic Perovskites: New Tricks for an Old Dog. *Chem. Sci.* **2014**, *5*, 4712−4715.
(92) Kieslich, G.; Sun, S.; Cheetham, A. K. An Extended Tolerance Factor Approach for Organic-Inorganic Perovskites. *Chem. Sci.* **2015**, *6*, 3430−3433.
(93) Travis, W.; Glover, E. N. K.; Bronstein, H.; Scanlon, D. O.; Palgrave, R. G. On The Application of the Tolerance Factor to Inorganic and Hybrid Halide Perovskites: a Revised System. *Chem. Sci.* **2016**, *7*, 4548−4556.
(94) Jeon, N. J.; Noh, J. H.; Yang, W. S.; Kim, Y. C.; Ryu, S.; Seo, J.; Seok, S. I. Compositional Engineering of Perovskite Materials for High-Performance Solar Cells. *Nature* **2015**, *517*, 476−480.
(95) Saliba, M.; Orlandi, S.; Matsui, T.; Aghazada, S.; Cavazzini, M.; Correa-Baena, J.-P.; Gao, P.; Scopelliti, R.; Mosconi, E.; Dahmen, K.-H.; De Angelis, F.; Abate, A.; Hagfeldt, A.; Pozzi, G.; Graetzel, M.; Nazeeruddin, M. K. A Molecularly Engineered Hole-Transporting Material for Efficient Perovskite Solar Cells. *Nat. Energy* **2016**, *1*, 15017.
(96) Li, X.; Bi, D. Q.; Yi, C. Y.; Decoppet, J. D.; Luo, J. S.; Zakeeruddin, S. M.; Hagfeldt, A.; Gratzel, M. A Vacuum Flash-Assisted Solution Process for High-Efficiency Large-Area Perovskite Solar Cells. *Science* **2016**, *353*, 58−62.
(97) Cho, K. T.; Paek, S.; Grancini, G.; Roldan Carmona, C.; Gao, P.; Lee, Y. H.; Nazeeruddin, M. K. Highly Efficient Perovskite Solar Cells with a Compositional Engineered Perovskite/Hole Transporting Material Interface. *Energy Environ. Sci.* **2017**, *10*, 621−627.
(98) Choi, H.; Jeong, J.; Kim, H. B.; Kim, S.; Walker, B.; Kim, G. H.; Kim, J. Y. Cesium-Doped Methylammonium Lead Iodide Perovskite Light Absorber for Hybrid Solar Cells. *Nano Energy* **2014**, *7*, 80−85.
(99) Saliba, M.; Matsui, T.; Seo, J. Y.; Domanski, K.; Correa-Baena, J. P.; Nazeeruddin, M. K.; Zakeeruddin, S. M.; Tress, W.; Abate, A.; Hagfeldt, A.; Gratzel, M. Cesium-Containing Triple Cation Perovskite Solar Cells: Improved Stability, Reproducibility and High Efficiency. *Energy Environ. Sci.* **2016**, *9*, 1989−1997.
(100) Phillips, T. W.; Lignos, I. G.; Maceiczyk, R. M.; deMello, A. J.; deMello, J. C. Nanocrystal Synthesis in Microfluidic Reactors: Where Next? *Lab Chip* **2014**, *14*, 3172−3180.
(101) Lignos, I.; Maceiczyk, R.; deMello, A. J. Microfluidic Technology: Uncovering the Mechanisms of Nanocrystal Nucleation and Growth. *Acc. Chem. Res.* **2017**, *50*, 1248−1257.
(102) Jensen, K. F.; Reizman, B. J.; Newman, S. G. Tools for Chemical Synthesis in Microsystems. *Lab Chip* **2014**, *14*, 3206−3212.
(103) Niu, G. D.; Ruditskiy, A.; Vara, M.; Xia, Y. N. Toward Continuous and Scalable Production of Colloidal Nanocrystals by Switching from Batch to Droplet Reactors. *Chem. Soc. Rev.* **2015**, *44*, 5806−5820.
(104) Nightingale, A. M.; Krishnadasan, S. H.; Berhanu, D.; Niu, X.; Drury, C.; McIntyre, R.; Valsami-Jones, E.; deMello, J. C. A Stable Droplet Reactor for High Temperature Nanocrystal Synthesis. *Lab Chip* **2011**, *11*, 1221−1227.
(105) Lignos, I.; Protesescu, L.; Stavrakis, S.; Piveteau, L.; Speirs, M. J.; Loi, M. A.; Kovalenko, M. V.; deMello, A. J. Facile Droplet-based Microfluidic Synthesis of Monodisperse IV-VI Semiconductor Nanocrystals with Coupled In-Line NIR Fluorescence Detection. *Chem. Mater.* **2014**, *26*, 2975−2982.
(106) Lignos, I.; Stavrakis, S.; Kilaj, A.; deMello, A. J. Millisecond-Timescale Monitoring of PbS Nanoparticle Nucleation and Growth Using Droplet-Based Microfluidics. *Small* **2015**, *11*, 4009−4017.
(107) Abolhasani, M.; Coley, C. W.; Xie, L. S.; Chen, O.; Bawendi, M. G.; Jensen, K. F. Oscillatory Microprocessor for Growth and *in Situ* Characterization of Semiconductor Nanocrystals. *Chem. Mater.* **2015**, *27*, 6131−6138.
(108) Abecassis, B.; Bouet, C.; Garnero, C.; Constantin, D.; Lequeux, N.; Ithurria, S.; Dubertret, B.; Pauw, B. R.; Pontoni, D. Real-Time *in Situ* Probing of High-Temperature Quantum Dots Solution Synthesis. *Nano Lett.* **2015**, *15*, 2620−2626.
(109) Xie, L. S.; Shen, Y.; Franke, D.; Sebastian, V.; Bawendi, M. G.; Jensen, K. F. Characterization of Indium Phosphide Quantum Dot Growth Intermediates Using MALDI-TOF Mass Spectrometry. *J. Am. Chem. Soc.* **2016**, *138*, 13469−13472.
(110) Epps, R. W.; Felton, K. C.; Coley, C. W.; Abolhasani, M. Automated Microfluidic Platform for Systematic Studies of Colloidal Perovskite Nanocrystals: Towards Continuous Nano-Manufacturing. *Lab Chip* **2017**, *17*, 4040−4047.
(111) Maceiczyk, R. M.; Hess, D.; Chiu, F. W. Y.; Stavrakis, S.; deMello, A. J. Differential Detection Photothermal Spectroscopy: Towards Ultra-Fast and Sensitive Label-Free Detection in Picoliter and Femtoliter Droplets. *Lab Chip* **2017**, *17*, 3654−3663.
(112) Shen, Y.; Roberge, A.; Tan, R.; Gee, M. Y.; Gary, D. C.; Huang, Y. C.; Blom, D. A.; Benicewicz, B. C.; Cossairt, B. M.; Greytak, A. B. Gel Permeation Chromatography as a Multifunctional Processor for Nanocrystal Purification and on-Column Ligand Exchange Chemistry. *Chem. Sci.* **2016**, *7*, 5671−5679.
(113) Shen, Y.; Gee, M. Y.; Greytak, A. B. Purification Technologies for Colloidal Nanocrystals. *Chem. Commun.* **2017**, *53*, 827−841.
(114) Shen, Y.; Abolhasani, M.; Chen, Y.; Xie, L.; Yang, L.; Coley, C. W.; Bawendi, M. G.; Jensen, K. F. *In-Situ* Microfluidic Study of Biphasic Nanocrystal Ligand-Exchange Reactions Using an Oscillatory Flow Reactor. *Angew. Chem.* **2017**, *129*, 16551−16555.
(115) Krishnadasan, S.; Brown, R. J. C.; deMello, A. J.; deMello, J. C. Intelligent Routes to the Controlled Synthesis of Nanoparticles. *Lab Chip* **2007**, *7*, 1434−1441.
(116) Orimoto, Y.; Watanabe, K.; Yamashita, K.; Uehara, M.; Nakamura, H.; Furuya, T.; Maeda, H. Application of Artificial Neural Networks to Rapid Data Analysis in Combinatorial Nanoparticle Syntheses. *J. Phys. Chem. C* **2012**, *116*, 17885−17896.

DOI: 10.1021/acsnano.8b01122
ACS Nano 2018, 12, 5504−5517

(117) Maceiczyk, R. M.; deMello, A. J. Fast and Reliable Metamodeling of Complex Reaction Spaces Using Universal Kriging. *J. Phys. Chem. C* **2014**, *118*, 20026−20033.
(118) Maceiczyk, R. M.; Bezinge, L.; deMello, A. J. Kinetics of Nanocrystal Synthesis in a Microfluidic Reactor: Theory and Experiment. *React. Chem. Eng.* **2016**, *1*, 261−271.
(119) Yashina, A.; Lignos, I.; Stavrakis, S.; Choo, J.; DeMello, A. J. Scalable Production of $CuInS_2$/ZnS Quantum Dots in a Two-Step Droplet-Based Microfluidic Platform. *J. Mater. Chem. C* **2016**, *4*, 6401−6408.
(120) Willmott, P. R.; Meister, D.; Leake, S. J.; Lange, M.; Bergamaschi, A.; Boge, M.; Calvi, M.; Cancellieri, C.; Casati, N.; Cervellino, A.; Chen, Q.; David, C.; Flechsig, U.; Gozzo, F.; Henrich, B.; Jaggi-Spielmann, S.; Jakob, B.; Kalichava, I.; Karvinen, P.; Krempasky, J.; et al. The Materials Science Beamline Upgrade at the Swiss Light Source. *J. Synchrotron Radiat.* **2013**, *20*, 667−682.
(121) Cervellino, A.; Frison, R.; Bertolotti, F.; Guagliardi, A. DEBUSSY 2.0: the New Release of a Debye User System for Nanocrystalline and/or Disordered Materials. *J. Appl. Crystallogr.* **2015**, *48*, 2026−2032.
(122) Protesescu, L.; Yakunin, S.; Bodnarchuk, M. I.; Bertolotti, F.; Masciocchi, N.; Guagliardi, A.; Kovalenko, M. V. Monodisperse Formamidinium Lead Bromide Nanocrystals with Bright and Stable Green Photoluminescence. *J. Am. Chem. Soc.* **2016**, *138*, 14202−14205.
(123) Schueller, E. C.; Laurita, G.; Fabini, D. H.; Stoumpos, C. C.; Kanatzidis, M. G.; Seshadri, R. Crystal Structure Evolution and Notable Thermal Expansion in Hybrid Perovskites Formamidinium Tin Iodide and Formamidinium Lead Bromide. *Inorg. Chem.* **2018**, *57*, 695−701.
(124) Giebink, N. C.; Forrest, S. R. Quantum Efficiency Roll-Off at High Brightness in Fluorescent and Phosphorescent Organic Light Emitting Diodes. *Phys. Rev. B: Condens. Matter Mater. Phys.* **2008**, *77*, 235215.
(125) Su, S.-J.; Sasabe, H.; Takeda, T.; Kido, J. Pyridine-Containing Bipolar Host Materials for Highly Efficient Blue Phosphorescent OLEDs. *Chem. Mater.* **2008**, *20*, 1691−1693.
(126) Yuan, M. J.; Quan, L. N.; Comin, R.; Walters, G.; Sabatini, R.; Voznyy, O.; Hoogland, S.; Zhao, Y. B.; Beauregard, E. M.; Kanjanaboos, P.; Lu, Z. H.; Kim, D. H.; Sargent, E. H. Perovskite Energy Funnels for Efficient Light-Emitting Diodes. *Nat. Nanotechnol.* **2016**, *11*, 872−877.
(127) Vashishtha, P.; Halpert, J. E. Field-Driven Ion Migration and Color Instability in Red-Emitting Mixed Halide Perovskite Nanocrystal Light-Emitting Diodes. *Chem. Mater.* **2017**, *29*, 5965−5973.
(128) Meier, S. B.; Tordera, D.; Pertegás, A.; Roldán-Carmona, C.; Ortí, E.; Bolink, H. J. Light-Emitting Electrochemical Cells: Recent Progress and Future Prospects. *Mater. Today* **2014**, *17*, 217−223.
(129) Xiao, Z. G.; Kerner, R. A.; Zhao, L. F.; Tran, N. L.; Lee, K. M.; Koh, T. W.; Scholes, G. D.; Rand, B. P. Efficient Perovskite Light-Emitting Diodes Featuring Nanometre-Sized Crystallites. *Nat. Photonics* **2017**, *11*, 108−115.
(130) Wang, N. N.; Cheng, L.; Ge, R.; Zhang, S. T.; Miao, Y. F.; Zou, W.; Yi, C.; Sun, Y.; Cao, Y.; Yang, R.; Wei, Y. Q.; Guo, Q.; Ke, Y.; Yu, M. T.; Jin, Y. Z.; Liu, Y.; Ding, Q. Q.; Di, D. W.; Yang, L.; Xing, G. C.; et al. Perovskite Light-Emitting Diodes Based on Solution-Processed Self-Organized Multiple Quantum Wells. *Nat. Photonics* **2016**, *10*, 699−704.
(131) Sanehira, E. M.; Marshall, A. R.; Christians, J. A.; Harvey, S. P.; Ciesielski, P. N.; Wheeler, L. M.; Schulz, P.; Lin, L. Y.; Beard, M. C.; Luther, J. M. Enhanced Mobility $CsPbI_3$ Quantum Dot Arrays for Record-Efficiency, High-Voltage Photovoltaic Cells. *Sci. Adv.* **2017**, *3*, eaao4204.
(132) Saran, R.; Curry, R. J. Lead Sulphide Nanocrystal Photodetector Technologies. *Nat. Photonics* **2016**, *10*, 81−92.
(133) Brouwer, A. M. Standards for Photoluminescence Quantum Yield Measurements in Solution (IUPAC Technical Report). *Pure Appl. Chem.* **2011**, *83*, 2213−2228.
(134) Forrest, S. R.; Bradley, D. D. C.; Thompson, M. E. Measuring the Efficiency of Organic Light-Emitting Devices. *Adv. Mater.* **2003**, *15*, 1043−1048.

DOI: 10.1021/acsnano.8b01122
ACS Nano 2018, 12, 5504−5517